Central Lancashire Online Knowledge (CLoK)

Title	Galaxy and mass assembly: accurate panchromatic photometry from optical priors using LAMBDAR
Type	Article
URL	https://clok.uclan.ac.uk/id/eprint/15109/
DOI	https://doi.org/10.1093/mnras/stw832
Date	2016
Citation	Wright, AH, Robotham, ASG, Borune, N, Driver, SP, Dunne, L, Maddox, SJ, Alpaslan, M, Andrews, SK, Bauer, AE et al (2016) Galaxy and mass assembly: accurate panchromatic photometry from optical priors using LAMBDAR. Monthly Notices of the Royal Astronomical Society, 460 (1). pp. 766-801. ISSN 0035-8711
Creators	Wright, AH, Robotham, ASG, Borune, N, Driver, SP, Dunne, L, Maddox, SJ, Alpaslan, M, Andrews, SK, Bauer, AE, Bland-Hawthorn, J, Popescu, Cristina and et al.

It is advisable to refer to the publisher's version if you intend to cite from the work.
https://doi.org/10.1093/mnras/stw832

For information about Research at UCLan please go to http://www.uclan.ac.uk/research/

Galaxy And Mass Assembly: accurate panchromatic photometry from optical priors using LAMBDAR

A. H. Wright,[1][⋆] A. S. G. Robotham,[1] N. Bourne,[2] S. P. Driver,[1,3] L. Dunne,[2,4]
S. J. Maddox,[2,4] M. Alpaslan,[5] S. K. Andrews,[1] A. E. Bauer,[6] J. Bland-Hawthorn,[7]
S. Brough,[6] M. J. I. Brown,[8] C. Clarke,[9] M. Cluver,[10] L. J. M. Davies,[1]
M. W. Grootes,[11] B. W. Holwerda,[12] A. M. Hopkins,[6] T. H. Jarrett,[13] P. R. Kafle,[1]
R. Lange,[1] J. Liske,[14] J. Loveday,[9] A. J. Moffett,[1] P. Norberg,[15] C. C. Popescu,[16,17]
M. Smith,[4] E. N. Taylor,[18] R. J. Tuffs,[19] L. Wang[20] and S. M. Wilkins[9]

Affiliations are listed at the end of the paper

ABSTRACT

We present the Lambda Adaptive Multi-Band Deblending Algorithm in R (LAMBDAR), a novel code for calculating matched aperture photometry across images that are neither pixel- nor PSF-matched, using prior aperture definitions derived from high-resolution optical imaging. The development of this program is motivated by the desire for consistent photometry and uncertainties across large ranges of photometric imaging, for use in calculating spectral energy distributions. We describe the program, specifically key features required for robust determination of panchromatic photometry: propagation of apertures to images with arbitrary resolution, local background estimation, aperture normalization, uncertainty determination and propagation, and object deblending. Using simulated images, we demonstrate that the program is able to recover accurate photometric measurements in both high-resolution, low-confusion, and low-resolution, high-confusion, regimes. We apply the program to the 21-band photometric data set from the Galaxy And Mass Assembly (GAMA) Panchromatic Data Release (PDR; Driver et al. 2016), which contains imaging spanning the far-UV to the far-IR. We compare photometry derived from LAMBDAR with that presented in Driver et al. (2016), finding broad agreement between the data sets. None the less, we demonstrate that the photometry from LAMBDAR is superior to that from the GAMA PDR, as determined by a reduction in the outlier rate and intrinsic scatter of colours in the LAMBDAR data set. We similarly find a decrease in the outlier rate of stellar masses and star formation rates using LAMBDAR photometry. Finally, we note an exceptional increase in the number of UV and mid-IR sources able to be constrained, which is accompanied by a significant increase in the mid-IR colour–colour parameter-space able to be explored.

Key words: techniques: photometric – astronomical data bases: miscellaneous – galaxies: evolution – galaxies: general – galaxies: photometry.

1 INTRODUCTION

Over the past decade, the existence of large multiwavelength collaborations such as the Galaxy and Mass Assembly (GAMA; Driver et al. 2011, 2016; Liske et al. 2015) survey, *Herschel* Astrophysical Terahertz Large Area Survey (H-ATLAS; Eales et al. 2010), *Herschel* Extragalactic Legacy Project (Vaccari & HELP Consortium 2015), the Cosmological Evolution Survey (COSMOS; Scoville et al. 2007), the Cosmic Assembly Near-infrared Deep Extragalactic Legacy Survey (Grogin et al. 2011; Koekemoer et al. 2011), and the Great Observatories Origins Deep Survey (Elbaz et al. 2011), has enabled scientists to probe an increasing array of extragalactic environments, and eras in an increasingly comprehensive and systematic manner.

One area of interest in multiwavelength extragalactic studies is the determination of self-consistent galactic parameters such as stellar mass (Taylor et al. 2011), dust mass (Dunne et al. 2011), and star formation rate measures (Davies et al. 2015). Using

⋆ E-mail: angus.wright@icrar.org

statistically robust samples of these parameters, we can populate global distributions of interest, such as the galaxy stellar mass function (Baldry et al. 2012) and evolution of the cosmic star formation rate (Madau & Dickinson 2014). By combining self-consistent measures of these distributions with H I mass estimates, we can examine the galactic baryonic mass function (Papastergis et al. 2012). While these individual parameters are able to be calculated to high accuracy without the fitting of complex models (indeed, adding more information than is explicitly necessary can act to detriment the measurement of individual parameters; see Taylor et al. 2011), in order to calculate these parameters self-consistently measurement of individual galactic spectral energy distributions (SEDs) is nominally best practice. This is because modelling the SED allows all galactic parameters to be optimized simultaneously with consideration of how they impact one-another and co-evolve (Walcher et al. 2011; Conroy 2013).

Measurement of these parameters requires quantification of the flux emitted by an object in one or more photometric images, and in particular the management of data with very different sensitivity limits and spatial resolutions. To measure total object fluxes robustly, it is important to determine a sensible metric of measurement, and then to quantify any flux systematically missed because of this chosen method. The simplest approach to measuring total object photometry involves using circular apertures to capture a known fraction of an object's flux, which can then be corrected to a total flux (Petrosian 1976; Kron 1980), or by extending these methods to elliptical apertures (Bertin & Arnouts 1996; Jarrett et al. 2000). Measurement can be refined by fitting observed structure when calculating photometry, either by assuming a fixed profile shape, e.g. an exponential profile (Patterson 1940; Freeman 1970), De Vaucouleurs (1948) profile, or by fitting for the profile shape using a generalized Sérsic profile (Sérsic 1963; Graham et al. 2005; Jarrett et al. 2013; Kelvin et al. 2014). These methods, however, can cause systematic underestimation of total fluxes as a function of morphology (Graham et al. 2005).

Unfortunately, there is no 'standard' photometric method that is used, or even necessarily able, to extract photometry from a wide range of photometric images (Hill et al. 2010; Driver et al. 2016). As a result, compilation of large samples of multiwavelength photometry is typically achieved in one of three ways: by using a cross-matching scheme that combines photometric measurements (often from different methods) at the catalogue level ('table matching', see e.g. Bundy et al. 2012); by degrading the resolution of all images to that of the lowest resolution image, and performing matched aperture photometry on these degraded images ('forced aperture photometry'; see e.g. Bertin & Arnouts 1996; Capak et al. 2007; Hill et al. 2010; Hildebrandt et al. 2012; Driver et al. 2016); or by using information in a high-resolution band to inform the extraction of photometry at lower resolutions, either by matching flux ratios ('flux fitting'; see e.g. De Santis et al. 2007; Laidler et al. 2007; Mancone et al. 2013; Merlin et al. 2015) or by matching structure ('profile fitting'; see e.g. Strauss et al. 2002; Kuijken 2008; Kelvin et al. 2012; Vika et al. 2013; Erwin 2014).

These methods of analysis each have benefits and detriments. 'Forced aperture photometry' is implemented widely but has limited use when the quality of images needing to be analysed varies significantly (Hill et al. 2011), as the method discards spatial information in the image degradation. 'Flux fitting' and 'profile fitting' are both very sophisticated, and are useful in cases where there exists a large disparity between photometric images and the highest resolution image is able to reliably determine object structure (Kelvin et al. 2012). In cases where it is not possible to reliably determine object

structure in all bands, however, one must propagate an observed profile in one band to lower resolution, often longer wavelength, images. As physical processes vary greatly as a function of wavelength, it is not clear how the profiles might be linked across such large wavelength regions. Accounting for this change across wavelength likely involves assuming complex models, which may not hold for arbitrary galaxy populations. Finally, 'table matching' is quick, easy, and requires no further analysis of photometric imaging (Bundy et al. 2012; Driver et al. 2016); however, it does not guarantee that individual measurements will be consistent across multiple facilities and/or wavelengths (see Section 2).

The point of consistency is an important one and is the reason why so much effort has been invested in developing programs for matched aperture, forced aperture, flux fitting, and profile fitting photometry. In order to model the SED of any object, photometric data are compared to physically motivated models of panchromatic emission that are either pre-constructed (as is the case in energy-balance programs; see e.g. Da Cunha, Charlot & Elbaz 2008; Boquien et al. 2013) or developed dynamically (as in radiative transfer programs; see e.g. Popescu et al. 2011; Camps & Baes 2015). In any case, it is assumed that the data have measurements and uncertainties that are consistent, so that no measurement is unfairly weighted with respect to any other during least-squares optimization. For the specific goals of GAMA, in particular the careful measurement of the SEDs from the UV to the far-IR (FIR), such consistency is vital. For this reason, we are required to conduct an analysis that is more sophisticated than simple table matching.

For this purpose, we have developed a bespoke program for calculating consistent photometry for objects across imaging with arbitrary resolutions, using prior information derived from a highest resolution band; the Lambda Adaptive Multi-Band Deblending Algorithm in R (LAMBDAR).

In Section 2, we discuss the GAMA photometric data set. In Section 3, we discuss the program and its many features, detailing the function of the more important or complex routines. Sections 4 and 5 detail our testing of the program on simulated optical and FIR imaging, respectively. Section 6 details the photometry that we measure for all GAMA objects, and how our measurements compare to those presented in the GAMA Panchromatic Data Release (PDR; Driver et al. 2016). In Section 7, we examine how the new photometry compares to the PDR with regard to derived galactic properties such as stellar mass and star formation rate. In Section 8, we detail the data release to accompany this publication. Finally, we present a summary and concluding remarks in Section 9.

2 THE GAMA PDR

Photometry in GAMA spans five different observatories, 21 different broad-band filters, and has pixel resolutions ranging from 0.4 to 12 arcsec. Each filter has its own characteristic point spread function (PSF), which in GAMA natively range in full width at half-maximum (FWHM) from 0.85 to 36 arcsec. Finally, each observatory typically implements a different image calibration scheme, specifically regarding estimation and removal of local sky-backgrounds.

With the exception of imaging in the *Herschel* 100 μm and 160 μm bands, the imaging used for measurement of photometry here is the same as that used in the GAMA PDR (Driver et al. 2016). Here we give a brief review of the photometry used in this analysis, and direct the interested reader to publications cited for detailed descriptions of the data and their genesis. A summary of the imaging properties in the GAMA PDR is given in Table 1.

Table 1. Details of the 21 bands included in the GAMA data base, and that are used for the creation of galactic SEDs. In the SDSS optical and VIKING NIR, the PSF FWHM values are shown for both the native imaging and the post-Gaussianized (i.e. convolved) imaging.

Band	Survey/ facility	Central wavelength	Pixel scale (arcsec)	Native (conv.) PSF FWHM (arcsec)
FUV	*GALEX*	1550 Å	1.5	4.1
NUV	*GALEX*	2275 Å	1.5	5.2
u	SDSS	3540 Å	0.339	1.4 (2.0)
g	SDSS	4770 Å	0.339	1.4 (2.0)
r	SDSS	6230 Å	0.339	1.4 (2.0)
i	SDSS	7630 Å	0.339	1.4 (2.0)
z	SDSS	9134 Å	0.339	1.4 (2.0)
Z	VIKING	8770 Å	0.339	0.9 (2.0)
Y	VIKING	1.020 μm	0.339	0.9 (2.0)
J	VIKING	1.252 μm	0.339	0.9 (2.0)
H	VIKING	1.645 μm	0.339	0.9 (2.0)
K	VIKING	2.147 μm	0.339	0.9 (2.0)
W1	*WISE*	3.4 μm	1	5.9
W2	*WISE*	4.6 μm	1	6.5
W3	*WISE*	12 μm	1	7.0
W4	*WISE*	22 μm	1	12.4
100	H-ATLAS	100 μm	3	9.6
160	H-ATLAS	160 μm	4	12.5
250	H-ATLAS	150 μm	6	18
350	H-ATLAS	350 μm	8	25
500	H-ATLAS	500 μm	12	36

Imaging in the UV domain is from The *GALaxy Evolution eXplorer* (*GALEX*; Martin et al. 2010) satellite, a medium-class explorer mission operated by NASA and launched in 2003 April. Data collected by *GALEX* in the GAMA equatorial fields was observed throughout both the medium imaging survey (MIS) and an additional dedicated survey, led by R.J. Tuffs, to MIS depth. *GALEX* imaging has a pixel resolution of 1.5 arcsec, and has a PSF FWHM of 4.2 and 5.3 arcsec in the far-UV (FUV) (153 nm) and NUV (230 nm) channels, respectively (Morrissey et al. 2007). *GALEX* imagery has approximately 92 and 95 per cent coverage in the equatorial fields. A detailed description of the GAMA *GALEX* data set is presented in Andrae (2014), and is summarized in Liske et al. (2015) and Driver et al. (2016).

The Sloan Digital Sky Survey (SDSS; York et al. 2000) provides uniform optical imaging in the GAMA equatorial fields in *ugriz* bands, at a pixel resolution of 0.4 arcsec and a typical PSF FWHM of 1.4 arcsec. Imaging used here is from SDSS DR7 data (Abazajian et al. 2009), and is described originally in Hill et al. (2011), updated in Liske et al. (2015). Importantly, the imaging used here has been Gaussianized to a PSF FWHM of 2 arcsec.

Near-IR (NIR) imaging is from the Visible and Infrared Telescope for Astronomy (VISTA; Sutherland et al. 2015), forming part of the VIsta Kilo-degree INfrared Galaxy survey (VIKING). VISTA has a pixel resolution of 0.4 arcsec, and a typical PSF FWHM of 0.85 arcsec. These data have also undergone Gaussianization to a common 2 arcsec PSF FWHM. While there is 100 per cent observational coverage from VISTA as part of the VIKING survey, quality control required that ∼2.2 per cent of the imaging frames be removed prior to mosaicking. As a result the final coverage varies slightly, but is typically better than 99 per cent in each of *ZYJHK*. Details of the VIKING quality control are given in Driver et al. (2016).

Mid-IR (MIR) imaging is from the *Wide-Field Infrared Survey Explorer* (*WISE*; Wright et al. 2010) satellite, a medium-class ex-

plorer mission operated by NASA and launched in 2009 December. Imaging used by GAMA has been 'drizzled' (see Jarrett et al. 2012; Cluver et al. 2014), reaching a final PSF FWHM of 5.9, 6.5, 7.0, and 12.4 arcsec in the *W*1 (3.4 μm), *W*2 (4.6 μm), *W*3 (12 μm), and *W*4 (22 μm) bands, respectively.

The *Herschel* space observatory (Pilbratt et al. 2010) is operated by the European Space Agency and was launched in 2009 May. Imaging used by GAMA from *Herschel* was observed as part of the H-ATLAS (Eales et al. 2010). H-ATLAS imaging in the GAMA equatorial fields utilises coordinated observations using both the PACS (Poglitsch et al. 2010) and SPIRE (Griffin et al. 2010) instruments to obtain scans at 100, 160, 250, 350, and 500 μm. Details of the imaging used are given in Valiante et al. (2016). Note that, due to ongoing investigation into the impact of the nebulizer scale on the final imaging properties, we opt to use the pre-nebulized maps for analysis here. Small-scale variations in the sky, which are removed by the nebulizer, are instead removed as part of the sky estimate routine; Appendix A shows an example of the small variations measured by the nebulizer compared to those measured by LAMBDAR.

Details of the methods for measuring photometry across all 21 bands in the PDR are given in Driver et al. (2016). Briefly, per-object photometry was collated in a number of ways. UV photometry from *GALEX* was calculated using a combination of aperture photometry and measurement using a curve of growth (CoG). Optical and NIR photometry from SDSS and VISTA were calculated by forced aperture photometry (Hill et al. 2011; Driver et al. 2016), using SEXTRACTOR (Bertin & Arnouts 1996). MIR photometry from *WISE* were calculated using a combination of aperture photometry and PSF modelling (Cluver et al. 2014). FIR photometry from the *Herschel* spacecraft were calculated using deblended, PSF-weighted aperture photometry (Bourne et al. 2012). Each of these data sets is subsequently table matched to create the final PDR photometric data set.

To demonstrate how multiwavelength table-matched photometry can produce incorrect measurements of the galactic SED, Fig. 1 shows a fit to inconsistent photometry as present in the GAMA PDR. This example shows inconsistency across instrument/facility boundaries (for example, the *GALEX*–SDSS boundary) but roughly consistent photometry within an instrument or facility's bandpass. While this has been chosen because it is a particularly dramatic case, we note that similar effects will be present at a lower level in all photometric measurements that are not made in a consistent manner across the entire frequency bandpass. We are therefore required to develop a method for measuring consistent photometry across the highly diverse GAMA PDR data set.

3 LAMBDAR: LAMBDA ADAPTIVE MULTI-BAND DEBLENDING ALGORITHM IN R

The LAMBDAR program is a development of a package detailed in Bourne et al. (2012). We have modified and evolved much of the internal mechanics, introduced scalability, and ported the program from IDL to an open source platform, R (R Core Team 2015).

The program has been designed for flexibility, scalability, and accuracy. LAMBDAR is available on the collaborative build network GitHub (https://github.com/AngusWright/LAMBDAR), to facilitate rapid updates. It is the hope of the authors that, by releasing the program publicly to the astronomical community, it will be tested, scrutinized, and hopefully improved, in a transparent and thorough fashion.
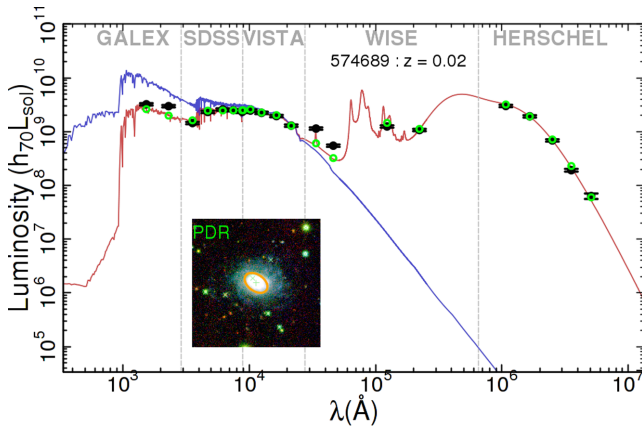
Figure 1. A simple example of how inconsistent photometry can result in incorrect measurement of the SED. Input photometry to the SED fit is shown in black, the model photometry in green, the obscured SED in red, and the unobscured SED in blue. For this object, the UV data were measured using an aperture which encompasses the entire galaxy, while the optical and FIR data have been measured in the shrunken aperture due to aperture shredding in SExtraction. This aperture is shown in the inset three-colour image (made using the VIKING H – SDSS i – SDSS g bands for red, green, and blue, respectively). The MIR data have been measured within a standard aperture with 8.25 arcsec radius. The SED has then been fit to the inconsistent photometry, giving the SED shown above.

The program is essentially a tool for performing aperture photometry. The user supplies a FITS image and a catalogue (containing object locations and aperture parameters), which the program uses to compute and output individual object fluxes. The program is designed to include functionality that incorporates behaviour similar to other matched aperture programs, such as the matched-aperture function within SEXTRACTOR, while allowing increased levels of sophistication and flexibility if desired. This is done for two reasons; first, it allows checks for consistency with other matched aperture codes; and secondly, to allow flexibility for the user to perform precisely the type of matched aperture photometry they require. Note that the LAMBDAR package does not perform a source detection, but rather requires an input catalogue of apertures (i.e. the 'priors', see Section 3.1).

In the following Sections (3.1–3.9), we outline the technical details of the program. The program follows the following broad process:

(i) read the required inputs, such as aperture priors and images (Section 3.1);

(ii) place input aperture priors on to the same pixel-grid as the image being analysed (Section 3.2);

(iii) convolve these aperture priors with the image PSF (Section 3.3);

(iv) perform object deblending using convolved aperture priors (Section 3.4);

(v) perform estimation of local sky-backgrounds (Section 3.5);

(vi) perform estimation of noise correlation using random/blank apertures (Section 3.6);

(vii) calculate object fluxes using deblended convolved aperture priors, accounting for local backgrounds (Section 3.7);

(viii) calculate and apply required normalization of fluxes to account for aperture weighting and/or missed flux (Section 3.8);

(ix) calculate final flux uncertainties, incorporating errors from each of the above steps (Section 3.9).

Additionally, individual routine descriptions (and instructions on how to run the program) are available in the package documentation. We direct the interested reader to the download page listed previously, where this and other documentation can be found. Alternatively, the reader can install the program directly into R using the following simple commands within the R environment:

```
install.packages('devtools')
library(devtools)
install_github('AngusWright/LAMBDAR')
library(LAMBDAR)
```

3.1 Inputs

The program does not perform an object detection, but rather requires an input catalogue from a source detection on the user's chosen 'prior' image. This list of prior targets remains static while analysing all images of interest; only a single source detection is required for the definition of prior targets. As such, for any successful flux measurement the user must specify (within the parameter file) at least:

(i) a catalogue of object right ascensions, declinations, and aperture parameters (semimajor axis, semiminor axis, position angle);

(ii) a FITS image with an unrotated tan gnomonic or orthographic World Coordinate System (WCS) Astrometry.

While the input catalogue need only contain the list of prior-based targets, it is often the case that we also want to mask and deblend contaminating sources which do not form part of the prior list. As such, the input catalogue can contain an additional parameter for identifying sources in the catalogue that are contaminants. However, as contaminating sources vary over a broad frequency range (e.g. stars in the optical, and high-redshift galaxies in the FIR), these additional sources often need to be tailored to specific images, separate to the static list of prior-based targets. Details of how these full catalogues are determined for GAMA are supplied in Section 6.2.

In addition to the required parameters, the user can specify any of a large number of optional parameters in order to perform various functions designed to improve the flux determination and/or allow for flexibility. Many of these parameters are discussed in the sections below, and all have descriptions within the program's documentation and default parameter file.

For reference, Table 2 outlines the parameter settings used in the GAMA run of LAMBDAR, as well as a short description of each parameters' purpose. We include a brief justification of these chosen settings in Section 6.3.

To create unrotated imaging, we choose to use the SWARP software (Bertin et al. 2002), and specify a MANUAL astrometric output.
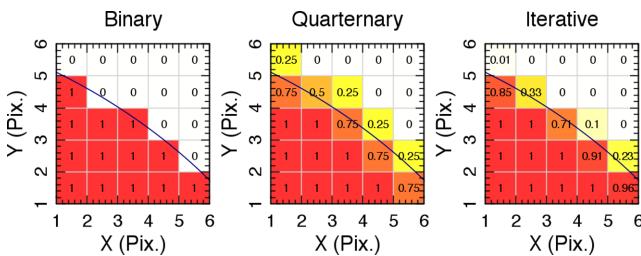
3.2 Aperture placement

When provided with the parameters required to define an elliptical aperture (as described above), how one goes about placing that aperture on a finite grid of pixels can be non-trivial. To allow for varying levels of complexity, LAMBDAR implements three different methods of placing elliptical apertures: binary, quaternary, and recursive descent aperture placement.

Given a 0-filled matrix/grid of pixels, binary aperture placement involves the allocation of 1s to all matrix elements (pixels) whose centres lie within the boundary of the elliptical aperture. For quaternary placement, pixels are valued as either $\{0, \frac{1}{4}, \frac{1}{2}, \frac{3}{4}, 1\}$, depending on how many corners of the pixel lie within the aperture boundary;

Table 2. Settings used in the GAMA LAMBDAR run. While this is not every setting in the program, these are all the settings that are of importance to the flux/error determination, discussed below, and/or set to a value that is not default.

Parameter	Setting	Caveats	Description
ResampleAper	TRUE	FALSE in SDSS/VIKING	Perform recursive descent aperture placement.
ResamplingRes	3		Resolution of each recursive descent step.
ResamplingIters	4		Number of recursive descent iterations.
PSFConvolve	TRUE		Perform a convolution of apertures with the PSF.
DoSkyEst	TRUE	FALSE in FUV only	Perform a local sky estimate for each source.
SkyEstProbCut	3		Sigma value used in clipping of sky pixels.
SkyEstIters	5		Number of sigma-clipping iterations in sky estimate.
BlankCor	TRUE		Estimate correlation in noise using blank apertures.
nBlanks	50		Number of blank apertures to measure for every source.
PSFWeighted	TRUE		Use 'weighted' apertures for flux measurements.
PixelFluxWgt	TRUE	FALSE from 12 μm redward	Use pixel-flux to weight apertures at the 0th iteration.
IterateFluxes	TRUE		Iteratively measure fluxes, weighting by mean surface brightness.
nIterations	15		Number of iterations to perform.

Figure 2. A demonstration of the three types of aperture placement that can be employed in LAMBDAR. The left-hand panel shows how aperture pixels are assigned using the binary aperture placement method; the centre panel shows pixel assignments using the quaternary aperture placement method; and the right-hand panel shows pixel assignments using the recursive descent method, implemented (by default) in LAMBDAR.

{0, 1, 2, 3, 4}, respectively. Finally, the quaternary method can be implemented recursively, such that pixels that are neither entirely inside nor outside the aperture are subdivided into smaller pixels, and are re-evaluated. The resultant subpixels are then summed together using their value multiplied by how many subdivisions down the tree they lie; i.e.

$$\int_0^r \int_0^{2\pi} A(r, \theta) \mathrm{d}r \mathrm{d}\theta \approx \sum_i \sum_j A(i, j) \times \frac{1}{(n \times d)}, \quad (1)$$

where n is the number of orders in the recursive descent, used in calculating the coverage of the (i, j)th pixel, and d is the degree of subdivision of the pixels, per step. These three methods of aperture placement are shown in Fig. 2.

Binary aperture placement is a very efficient and effective method of defining apertures provided that the size of the aperture, compared to the resolution of the grid, is large. As this is often not the case, using quaternary or iterative placement is recommended. In practice, however, systematic effects induced by the choice of aperture placement are small, and can be mitigated entirely by implementing aperture corrections (discussed at length in Section 3.8). LAMBDAR allows the user to choose which placement method is best suited to their imaging. For GAMA imaging, we use quaternary aperture generation, with recursive descent implemented in all but the highest resolution bands (see Table 2).

3.3 PSF convolution

After aperture placement, the program performs a convolution of the aperture with the PSF of the image being analysed. Convolution of apertures and point sources occurs after both the aperture and PSF have been placed on the same pixel grid as the image being analysed. Conversely, in real observations the convolution of an object's emission with the PSF happens prior to pixelization. This introduces a fundamental difference in how we treat objects approaching the point source limit, and how they behave under observation. As such, we identify the impact of this treatment, and how it affects the program's flux measurements.

The problem with performing pixelization before convolution is that it is possible to lose positional information during pixelization. As soon as an aperture has any axis that fails to cover multiple pixels, its effective centre will artificially shift to the pixel centre, and information will be lost. This is particularly problematic in images where pixels are large (compared to the aperture definitions). As such, we define the set of sources that can be adversely affected by performing the pixelization before convolution as those with aperture minor-axis smaller than half the image pixel diagonal:

$$r_\mathrm{m} \leq \Delta p \frac{\sqrt{2}}{2}. \quad (2)$$

Below this limit, aperture positional information may be lost under pixelization. To account for this loss of information, we do not actively convolve apertures below this limit with the PSF. Instead, we simply duplicate the PSF and interpolate it on to the same subpixel centroid as the source in question.

Above this limit, the aperture is Nyquist sampled under pixelization, and subsequently positional information cannot be lost. As such, for these sources we are able to create the normalized PSF convolved aperture model, $M_i(x, y)$, from the PSF function, $f_\mathrm{PSF}(x, y)$, and the prior aperture function, $f_\mathrm{ap,i}(x, y)$, as

$$M_i = \mathrm{Re}\left[\mathcal{F}^{-1}(S)/n_S\right] \quad (3)$$

where

$$S = \mathrm{Mod}\left[\mathcal{F}(f_\mathrm{PSF})\right] \times \mathcal{F}(f_\mathrm{ap,i}), \quad (4)$$

$\mathcal{F}(f)$ is the Fourier transform of f, $\mathcal{F}^{-1}(f)$ is the inverse Fourier transform of f, $\mathrm{Mod}[f]$ is the complex modulus of f, $\mathrm{Re}[f]$ is the real-part extraction of f, and n_S is the number of pixels in the image S.

The complex modulus in this equation serves the purpose of removing the spatial information of the PSF after convolution, thus

ensuring all positional information of the convolved aperture originates from the aperture itself, and is not impacted by whether the supplied PSF is centred on a pixel centre, pixel corner, or anywhere in-between. This application of the complex modulus can adversely affect the structure of the PSF, particularly in cases where the PSF contains discrete steps in flux or multiple frequency components with different spatial centres. However as this is not typically the case with observational PSFs, we opt to perform the complex modulus (and therefore correct for possible PSF centroid issues) while acknowledging the limitations of this implementation. Furthermore, we test all the PSFs that are empirically determined in GAMA for adverse effects caused by the above. We find that there is typically a small residual (of a few per cent or less in the brightest pixels) between the pre- and post-convolution PSF, but that this residual is dominated by the centroid shift that the modulus is designed to introduce.

3.4 Object deblending

After convolution of the apertures with the PSF, the program performs a complex deblending of sources. LAMBDAR implements a method of deblending whereby flux in any given pixel is fractionally split between all sources with aperture models within that pixel. In order to accurately determine how much flux belongs to a given object, in any pixel, we make a few simple assumptions. First, the PSF-convolved aperture models, $M_i(x, y)$, are assumed to be a tracer of the emission profile of each source (for the purposes of deblending only). Secondly, we can define the total modelled flux of any given pixel, $T(x, y)$, as the sum of all n object models, evaluated at that pixel:

$$T(x, y) = \sum_i M_i(x, y). \tag{5}$$

Using this total modelled flux, we can define the fractional contribution of the ith model, at pixel (x, y), as

$$W_i(x, y) = \frac{M_i(x, y)}{T(x, y)}. \tag{6}$$

We call $W(x, y)$ the deblending weight function. Combining these two formulae, we define the ith 'deblended' model as

$$D_i(x, y) = M_i(x, y)W_i(x, y). \tag{7}$$

Using this model, we are able to calculate the flux of individual objects in the blended regime:

$$F_i^{D} = \sum_{x,y} (D_i(x, y) \times I(x, y)), \tag{8}$$

where $I(x, y)$ is the data image. Note that this prescription is identical to using the deblend weight function to create a 'deblended image':

$$I_i^{D}(x, y) = W_i(x, y)I(x, y), \tag{9}$$

and then simply applying the original model $M_i(x, y)$ to this image. In terms of description, the former is more useful for calculating uncertainties and corrections on aperture fluxes, and is used in Section 3.8. Conversely, the latter makes more sense intuitively, and as a result we often choose to show it in visualizations. For example, Fig. 3 demonstrates the deblending process using this latter description of the deblending procedure. In the figure, we simulate two point sources (with equal flux) in a low-resolution image that are separated by less than the PSF FWHM (and which are therefore unresolved). Using the high-resolution priors ($f_{ap,i}$, first panel), which we then convolve with the low-resolution PSF to
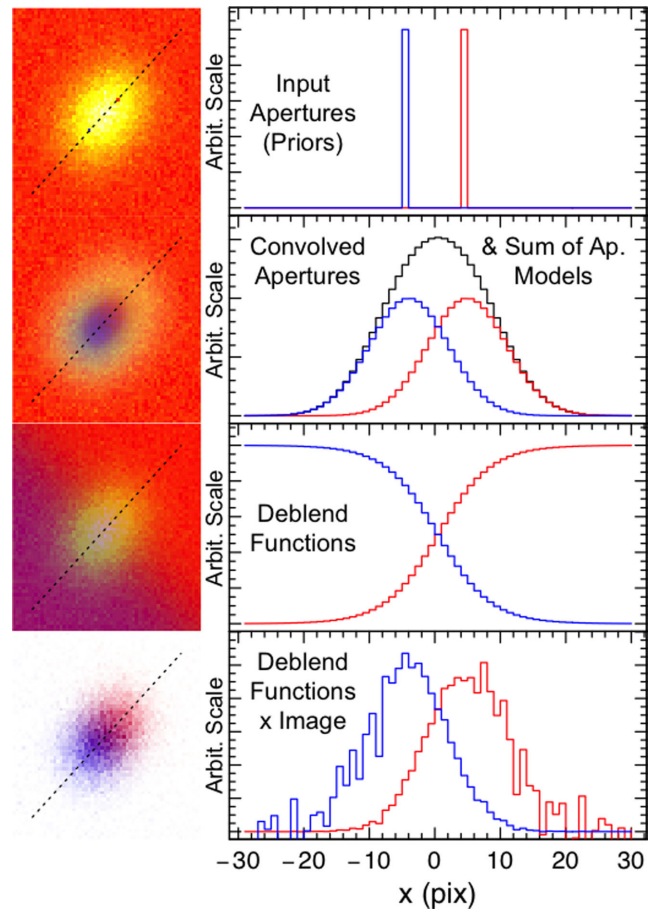

Figure 3. Demonstration of how deblending of apertures is performed. Two point sources (i.e. objects perfectly modelled by the PSF) were simulated using an example PSF and noise profile (image top left). Model parameters for two point sources are provided to the program, at the known locations of the two objects (thereby simulating use of a known optical prior; top right). Using these priors, and the known PSF, models for the two sources are generated (second row). The deblend function for each object is determined by the ratio between each model and the sum of all models (third row). The image is then deblended for each object, through multiplication by the deblend function (fourth row). This final image is then used for flux measurement, using the user-desired measurement method (see Section 3.7). In each row, the right-hand column shows the slice through the left-hand image along the dotted black line.

create the aperture models (M_i, second panel), we can then calculate the deblend weights (W_i, third panel) for each object. This is done by dividing the aperture model (M_i, the red and blue lines in the second panel, respectively) by the sum of all models (T, the black line in the second panel). Finally, we multiply the simulated image, I, by the deblend weights to generate the deblended image (I_i^{D}, bottom panel).

3.4.1 Flux weighting and iterative deblending

The process of deblending objects can be improved when an additional object weighting mechanism is applied to objects, such as weighting based on relative surface brightness. The program allows this additional weighting in three ways. First, it allows initially unweighted models to be refined (using information from the image being analysed) through iteration, where the previous iteration's measured mean surface brightness per pixel is used as a weight
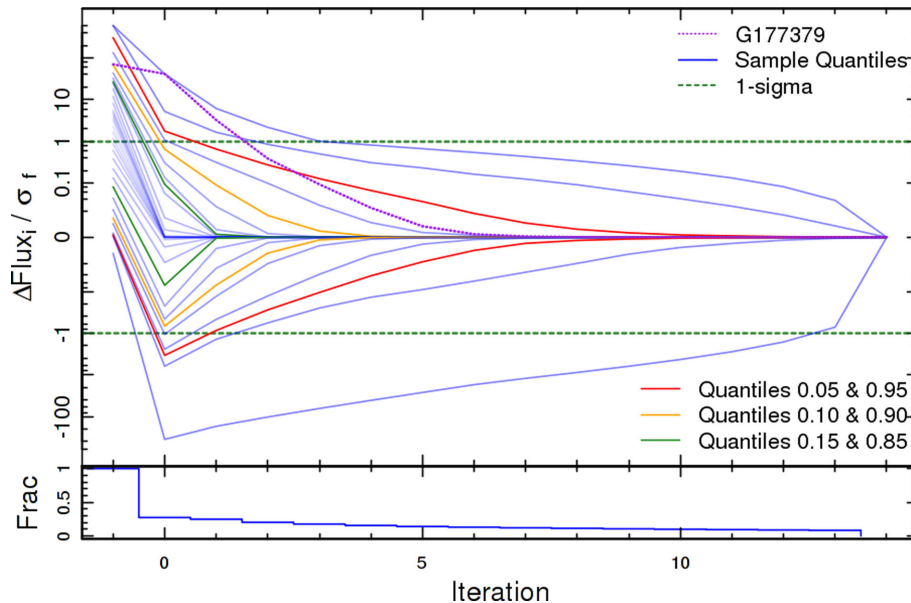
Figure 4. Demonstration of the convergence of flux iteration in the program for a sample of 953 blended galaxies located in 1 deg^2 centred on G177379 (shown in purple). At each iteration, we calculate a residual between every object's flux and the final measured flux. We then normalize these residuals by the final flux uncertainty, σ_f. We draw lines showing the distribution of 30 evenly distributed quantiles (from 99 to 1 per cent), as a function of iteration. The outermost 10, 20, and 30 per cent are highlighted with red, orange, and green lines, respectively. Here the -1th iteration is the flux measured in a blended aperture, the 0th iteration is that measured in an aperture whose deblend is based solely on the object apertures and their on-sky positions (i.e. it does not incorporate flux information), and subsequent iterations are deblended according to iterative average surface brightness. The histogram beneath the main figure shows the fraction of sources that have yet to converge at each iteration, as determined by whether their flux at the ith iteration is not equal to the final estimate. We see that the majority (i.e. $\geq$95 per cent) of fluxes have converged to within 1σ of their final estimate within five iterations.

for the subsequent iteration. Secondly, it allows users to use the central-pixel-flux of each object as a weight. Finally, it allows users to specify their own input weights, allowing, for example, information from other bands to influence flux measurements. Each of these methods has benefits and detriments, and it is often useful for the user to explore multiple options when attempting to extract the best photometry from their data. The program allows users to combine the latter two weighting options with the iterative improvement mechanism, and outputs fluxes measured at each stage of the iteration. An important caveat to the iterative flux determination procedure is the behaviour when an object is measured to have a flux less than or equal to zero. As these objects are deemed to have no contribution to the flux in the image, their weights are set to zero and the object is effectively discarded. It is not possible for the objects to return to the measurement space after being assigned a weight of 0, as no further measurements take place. These objects are assigned the flux as measured at the last iteration (prior to being discarded), and a photometry warning in the catalogue accompanies the measurement. Examples of the iterative deblending process are provided in Appendix B, for a range of blended-object flux ratios. As this is a simple example, we also note that a real, complex deblend is shown (in 2D) in panel 'd' of Fig. 5 (this figure is discussed at length in Section 3.4.2).

As described in the section above, the program optionally uses an iterative deblending of object apertures, based on the measured object average surface brightnesses. Fig. 4 shows the impact of this procedure for 953 galaxies in the GAMA SDSS r-band imaging. These galaxies are all located within 1 deg^2, centred on our example galaxy G177379. In this figure, we demonstrate the impact of iterated deblending on the convergence (as a population) of object fluxes as a function of iteration. We calculate the residual between every object's flux at the ith iteration and its final flux (measured

at the 15th iteration), normalized by the object's final uncertainty. We then calculate 60 evenly distributed quantiles (from 99 per cent to 1 per cent) for the population of all objects, and draw contours along these quantiles. From this figure, we can see that by iteration 5 all but the most extreme few per cent of objects are converged to within the uncertainty of their final flux.

3.4.2 Quantifying deblend solutions using CoG analysis

In order to demonstrate the importance and effectiveness of our deblend method, the program has the ability to output a CoG for each catalogued object. A CoG is a description of enclosed flux as a function of radius. In the program, CoGs are output as a diagnostic that can be used to investigate deblend solutions or galaxies that appear to have anomalous photometry. Currently CoGs are not used to assist with flux determination, however this addition is likely to occur in the near future.

An example of CoG output is shown in Fig. 5, where we show the GAMA object G177379, which is contaminated by a nearby bright star. In the figure, we show the image for our sample object (panel 'a') with the location of sources within the image, and colouring to show the object's model aperture and which pixels were used in measuring the sky estimate for this source. In panel 'b' we show the CoG for this source, both with and without deblending of nearby sources. In panel 'c' we show the deblended image I_i^D for this source, and include an estimate of the object's deprojected, deblended, half-light radius. Finally, panel 'd' shows the 2D deblend weights for this source, and is coloured by what is within the object's aperture. The impact of contamination on the CoG prior to deblending is evident, with large steps in the flux integral as a function of radius clearly apparent. After deblending, however, the
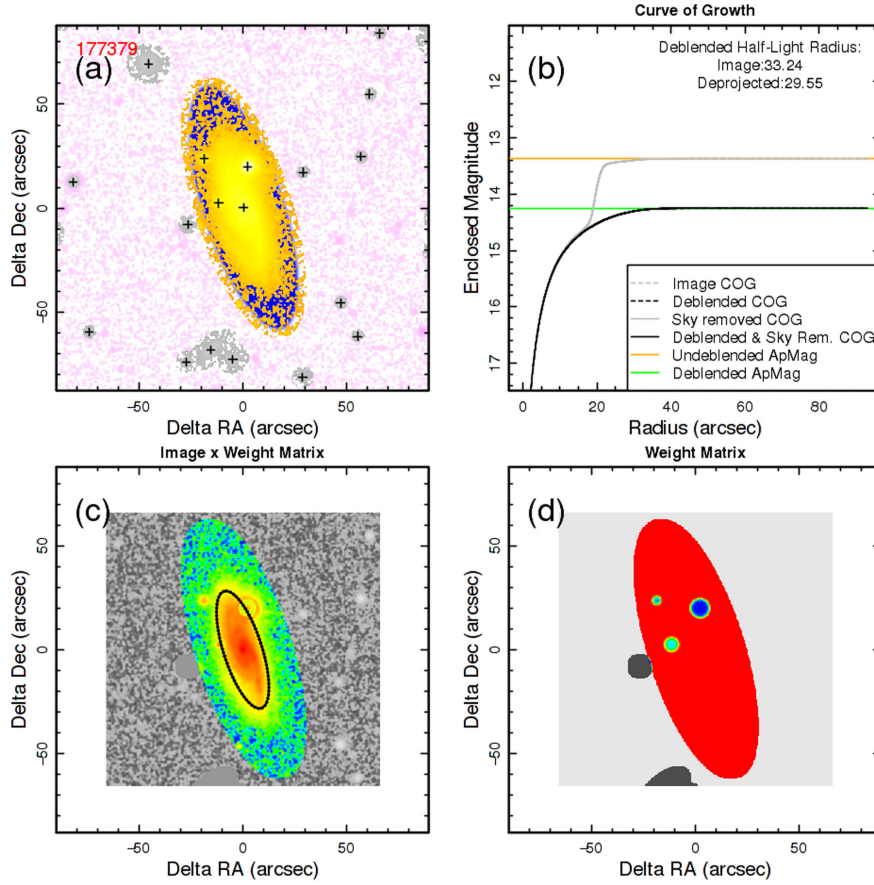
Figure 5. A demonstration of the impact of object deblending on the CoG flux of GAMA object G177379. Panel (a) shows the input image (grey-scale), with object aperture beneath in blue. Positive flux within the aperture is shown in yellow. Pixels deemed to be part of the 'sky' are shown in pink. Panel (b) shows the object CoG. The grey lines show the object CoG without deblending, and the black lines show the CoG with deblending (here the dotted lines are not visible as they are immediately behind the solid lines). Horizontal orange and green lines mark the measured aperture magnitude for the object before and after deblending, respectively. The text in the panel describes the circular and deprojected half-light radii, in arcseconds, with the deprojection being based on the input aperture (prior to convolution). Panel (c) shows the image stamp after deblending. Coloured pixels mark those within the object aperture, and grey-scale pixels mark those beyond the aperture. The black dotted line marks the measured deblended and deprojected half-light radius, as described in panel (b). Panel (d) shows the deblend weights for this object. Again, coloured pixels mark those within the aperture, and grey-scale pixels mark those beyond. Essentially, the grey and black CoGs in panel (b) are the radial integrals of panels (a) and (c), respectively. This four-panelled figure is a data-product optionally output by the program.

CoG is much more well behaved and plateaus to a final flux without large steps.

3.4.3 Quantifying deblend uncertainty

Finally, the program incorporates an uncertainty term to quantify the confidence in a deblend solution, ΔW_i. This deblend uncertainty term is of the form

$$\Delta W_i = \left[1 - \frac{\sum\limits_{x,y} D_i(x, y)}{\sum\limits_{x,y} M_i(x, y)} \right] \times \mathcal{D}, \qquad (10)$$

where $\mathcal{D}$ is the 'deblend uncertainty factor'. We chose to use

$$\mathcal{D} = \frac{1}{\sqrt{12}} \times |F_i^{\mathrm{M}}| \qquad (11)$$

where F_i^{M} is the flux measured within the ith source aperture prior to deblending, defined as $\sum\limits_{x,y} (M_i(x, y) \times I(x, y))$. This is the -1th

iteration shown in Fig. 4. Here $I(x, y)$ is the data image. The definition of the deblend uncertainty is such that an object that is determined to contribute 0 flux to the image (and which therefore has a $\sum\limits_{x,y} D_i(x, y) = 0$), will be given an uncertainty of $1/\sqrt{12}$ times the blended flux in the aperture. The factor $1/\sqrt{12}$ is the standard deviation (SD) of the uniform distribution over $U \in [0, 1]$, which is used to incorporate the (conservative) assumption that the distribution of deblend fractions is uniform over [0, 1]. This will not be the case (in fact, the distribution likely follows a beta distribution; see Cameron 2011), but we none the less choose to use this uniform approximation to be conservative. The result is that, for highly deblended sources, our deblend uncertainty is likely slightly overestimated.

3.5 Sky estimate

An important step in any aperture photometry measurement is a reliable determination of the local sky-background around each aperture. As such, LAMBDAR has an internal routine for determining the local sky-background around every aperture provided to the
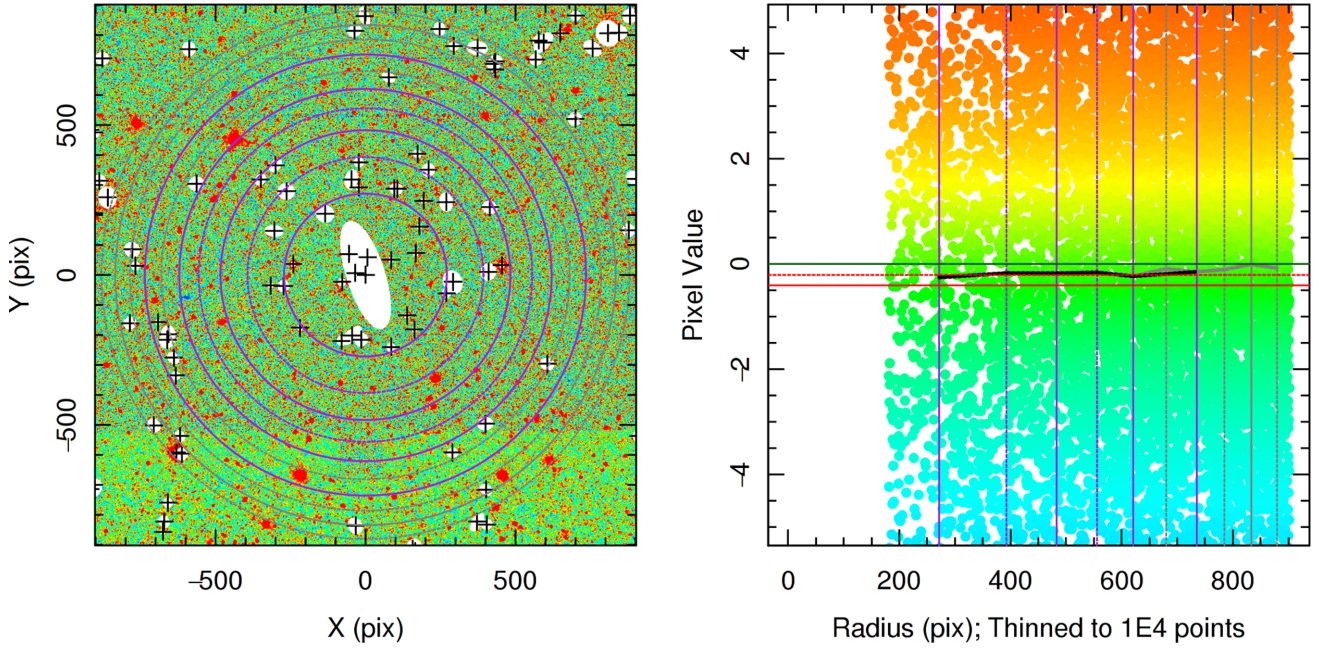
Figure 6. Demonstration of the sky estimate measured around GAMA object G177379 in the SDSS *r* band. The left-hand panel shows the image, masked pixels are shaded in black. In the right-hand panel, pixels values are shown as a function of radius, with the range on the *y*-axis set to be twice the measured sky RMS (which is 4.76 ADU for this object and image). The black lines show the binned running median (solid) and the uncertainty on the median (dashed). Here the uncertainty is small, so the dashed line is hard to distinguish from the solid. Horizontal red lines indicate the sky estimate using mean (solid) and median (dashed) statistics. The horizontal dark green line indicates the 0-line, for reference. Both panels are coloured by pixel values, on the same scale, and bin centres used in the estimate are shown as alternating solid and dashed purple/grey lines. Purple bins correspond to those whose means are within 1σ of the final sky estimate, and grey are those outside 1σ (and so were discarded when calculating the final estimate; See Section 3.5). This two-panelled figure is a data-product optionally output by the program.

program, and returns relevant information such as the mean and median sky values, the associated median absolute deviation (MAD) root-mean-squares (RMSs), and the Pearson chi-square normality test *p*-value. In this way, the function provides an indication of the local sky value, its uncertainty, and a quantification of the sky's Gaussianity.

In order to ensure that the function returns an accurate measure of the sky and is not contaminated by object flux, the program performs both a masking of all catalogued objects and (by default) an aggressive sigma-clipping of sky pixels. After masking and sigma-clipping, the program bins pixels into 10 radial bins (such that each bin contains an equal number of unmasked pixels). The radii are arranged with minimum bin edge at a radius equal to the object semimajor axis length, and the largest bin edge at 10 times this radius. In addition, the bins have hard minima and maxima, such that the innermost bin-edge is at least 3 PSF FWHM from the object centre and the outermost bin edge is at least 10 PSF FWHM from the object centre. If an aperture occupies a large fraction of the image, such that the largest bin radius would extend beyond the image edge, the function will generate the 10 equal-*N* bins using the pixels between the lower bin radius and the image edge. After binning using both a mean and median, the program then calculates the weighted mean of each to determine the sky estimate. When performing the weighted mean, the program uses weighting in both the confidence on the bin's individual mean/median, and in distance from the aperture centre:

$$w_i = [r_{i,\text{cen}} \times \sigma_i]^{-1} \qquad (12)$$

with $r_{i,\text{cen}}$ is the central radius of the *i*th bin, and σ_i is the uncertainty on the bin's mean/median. As such, the estimate is weighted to be

more representative of bins with better estimates and at lower radii. The uncertainty on the estimate is the SD of the binned values, without weighting (and thus, is the largest possible uncertainty). If there exist bins whose values are beyond the measured 1σ limit of the sky, these bins are discarded and the sky estimate recalculated. Finally, the program determines the number of bins that are within 1σ of the final sky estimate, and returns this diagnostic for reference of the user. Fig. 6 shows an example of the sky estimate and diagnostic images output by the program. The figure shows GAMA object G177379 imaged in the SDSS *r* band, the binned values for this galaxy, and the estimate for this object. Note the masked pixels in the image and the grey bins that have mean/median beyond the 1σ of the final estimate (and were therefore discarded). In this example, we can see that bins which have been excluded from the sky estimate are those which have been contaminated by pixels with different noise properties, from an adjacent stripe. In Section 4.2.1, we demonstrate that the sky estimate routine is robust to strong gradients in the sky, and variations in the uniformity of the sky RMS.

3.6 Randoms/blanks estimation

A measurement of the local sky, as described in Section 3.5, fails to account for correlations in the sky (which can systematically impact the actual sky RMS as a function of aperture geometry). As such, the program has two mechanisms for accounting for correlations in sky pixels around objects of interest: users can simply specify a multiplicative sky-correlation factor in the parameter file, or the program can perform a per-object randoms/blanks estimation. The multiplicative factor is used to increase the measured sky-error from

the previous section to reflect the impact of correlations, whereas the randoms/blanks estimations uses each object's aperture to empirically measure the correlated sky noise around the object.

The randoms/blanks estimation is calculated for every aperture by taking the masked image stamp $I_i^m(x, y)$ and transposing it in x and y as determined by quasi-random draws from a uniform distribution with boundaries $[0, N_{x,y}]$, where $N_{x,y}$ is the width of the image stamp in pixels in x and y. Using this transposed image stamp $I_i^m(x^*, y^*)$, the program measures the post-masking aperture-weighted flux at that point;

$$f_i = \sum_{x,y} I_i^m(x^*, y^*) \times M_i^m(x, y), \tag{13}$$

where $M_i^m(x, y)$ denotes the object aperture after removal of masked pixels. To calculate the final mean the program performs this measurement $N_{\rm rand}$ times and then calculates the weighted mean and unbiased weighted SD, using the following equations, respectively:

$$F_b = \frac{\sum_i f_i \times T_i^m}{\sum_i T_i^m}, \tag{14}$$

$$\sigma_b = \sqrt{\frac{\left(\sum_i T_i^m \times (f_i - F_b)^2\right) \times \left(\sum_i T_i^m\right)}{\left(\sum_i T_i^m\right)^2 - \sum_i (T_i^m)^2}}, \tag{15}$$

where $T_i^m = \sum_{x,y} M_i^m(x, y)$. In addition to these, the program also returns an independently calculated weighted MAD, $\sigma_{b,\rm mad}$. The reason for the inclusion of a MAD based $\sigma_{b,\rm mad}$ is that the SD determined can sometimes be unreasonably overestimated. SDs calculated via the MAD provide a more conservative measurement that is less impacted by outliers. In the case of Gaussian noise, the MAD is related to the standard deviation: $\mathrm{SD} = \mathrm{MADRMS}/\Phi^{-1}(\frac{3}{4}) \approx 1.4826 \times \mathrm{MADRMS}$, where $\Phi^{-1}(P)$ is the inverse of the cumulative distribution function of the normal function. This conversion is performed internally. By providing both the weighted MAD derived SD and the unbiased weighted SD, the program provides a check for the validity of the SDs. In the case of blanks, it also returns the number of blank apertures for which a post-masking aperture-weighted flux was successfully measured (because of heavy masking in crowded areas, entire apertures can be masked and hence provide no information). The randoms estimation and blanks estimation differ only in that the blanks estimation masks all catalogued sources in the image stamp before calculation, while the randoms function masks out only the object for which the correction is being calculated. This is done because the program uses image cutouts which are, by definition, centred on a source. As a result, randoms can be biased from being true reflections of random apertures because of this systematic image cropping.

As a result of the masking of all catalogued objects, the blanks estimation provides fundamentally different information to the randoms estimation. The blanks estimation details the flux contained within this aperture when placed over a part of the image that contains no sources brighter than the catalogue limit (and is therefore believed to be sky), whereas the latter details the flux contained in this aperture when randomly placed on the image, agnostic of all sources (catalogued or otherwise). The distinction between randoms and blanks is a useful one, as a comparison of randoms and blanks
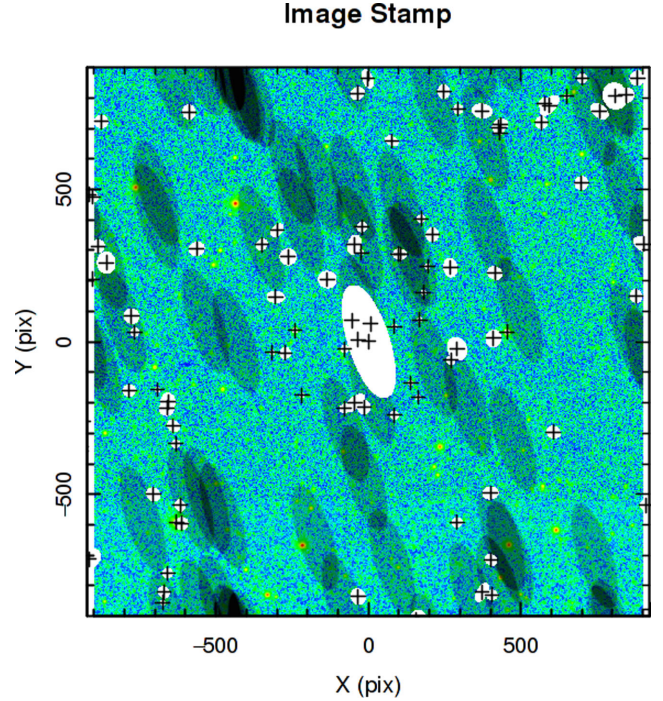
Figure 7. Demonstration of how blanks are measured within the program, using GAMA object G177379 in the SDSS r band as an example. Blank apertures are shaded in black (darker shades highlight pixels that went into multiple randoms). Masked pixels are white. The total flux in each blank aperture is measured, corrected for masking, and is used to calculate the weighted mean and SD blank flux for this source, which is returned in the final catalogue. This figure is a data-product optionally output by the program, and is useful for diagnostic checks.

can indicate the influence of source masking on your correlated-noise estimate. If the randoms and blanks return equivalent SDs, then this can indicate that the input catalogue is too shallow for reliable sky-estimation, or that you are masking the wrong pixels (i.e. your catalogue has been improperly defined for the image being analysed).

Additionally, measurement of the aperture flux values means that the randoms/blanks routine can also provide a rudimentary check for the measured sky estimate. An example of the blanks estimation is shown in Fig. 7, performed on a convolved SDSS r band image. Comparing this to the sky estimate for this same object (and band) shown in Fig. 6, the annular sky estimate returns a mean sky value of -0.20 ± 0.07 ADU per pixel, with a pixel-to-pixel RMS of 4.76 ADU. Conversely, the blanks estimation returns an effective mean pixel value of 0.73, with an effective pixel-to-pixel MAD RMS of 72.39 ADU (using 50 blanks). This suggests that, at this aperture scale, pixel-to-pixel correlations reduce the number of effective samples of the noise measured within the aperture by a factor of 15.21. We expect correlations in the SDSS background to be present because of our process of Gaussianization, and we can estimate that there should be correlations on the same order as the area of the Gaussianization kernel. A reduction in effective samples on the order of 15 times requires a Gaussian convolution kernel with FWHM ≤ 1.5 arcsec, which is the domain of the convolution kernel which was used. As such, we believe this to be a successful verification of the procedure.

3.7 Flux calculation

Once the deblended model has been determined, the next step is to convert the model aperture shown in Fig. 3 to the form desired for calculation of flux. The program is able to perform two types of flux measurement: simple aperture photometry and profile-weighted photometry.

For performing simple aperture photometry, the program uses the model aperture generated after convolution, $M_i(x, y)$, and converts it back to standard boxcar form. To achieve this, a user defined aperture fraction, $f \in (0, 1]$, is used. The aperture model is integrated outward until the point where f of the aperture is contained, and at this point a binary cut is imposed; all pixels with value greater than or equal to the pixel value at the cut point are given value 1, and all pixels with values lower are given value 0. This converts the model aperture from being a constantly varying aperture with domain $M_i(x, y) \in [0, 1]$, to being a boxcar-like aperture with domain $M_i^*(x, y) \in \{0, 1\}$. This binary aperture is then multiplied by the deblending weighting function, $W_i(x, y)$, giving the final deblended aperture $D_i(x, y) \in [0, 1]$. The image is then simply multiplied by final aperture and summed to return the deblended object flux, F_i^D:

$$F_i^D = \sum_{x,y} (D_i(x, y) \times I(x, y)). \tag{16}$$

In the case of isolated objects, i.e. where $W_i(x, y) = 1 \ \forall \ (x, y)$, $D_i(x, y) = M_i^*(x, y)$, and F_i^D is simply the sum of the aperture multiplied by the image.

For weighted photometry, the program skips the step of converting the aperture back to its standard boxcar form; i.e. $M_i^*(x, y) = M_i(x, y)$. Instead, the program uses the aperture model as a weighting function to extract a measurement. This allows for more reliable detections in cases where flux may otherwise be swamped by noise (particularly in the point-source limit). A demonstration of the different measurement methods can be seen in Fig. 8. The use of the weighting function is then corrected for using an aperture normalization detailed in Section 3.8.

After the flux measurement, the program subtracts the sky estimate measured in Section 3.5. This is simply the deblended flux F_i^D minus the sky-flux within the aperture: $F_i^s = f_s \times \sum_{x,y} M_i^*(x, y)$. The uncertainty on the flux is discussed in Section 3.9.

3.8 Aperture normalization

When performing aperture photometry, it is important to consider the impact of the choice of aperture weighting and size on the final photometric measurement. In the zero-noise regime, we want a measurement such that the choice of aperture weighting, and any aperture truncation, has no impact on the final object flux. In order to achieve this, the program normalizes aperture fluxes to account for any use of weighting or truncation. This normalization is akin to a traditional aperture correction for missed flux when performing simple aperture photometry, and to a weighting normalization when performing weighted aperture photometry. In practice, calculating the required correction/normalization can be done using a single method, regardless of measurement type.

The program calculates two different factors that can be used to normalize the measured fluxes. To calculate the factors, the program makes two limiting assumptions about the distribution of source flux. The first factor, denoted the 'maximum correction', assumes that the distribution of source flux follows exactly the shape of the object model (i.e. a PSF in the point source limit, and an aperture
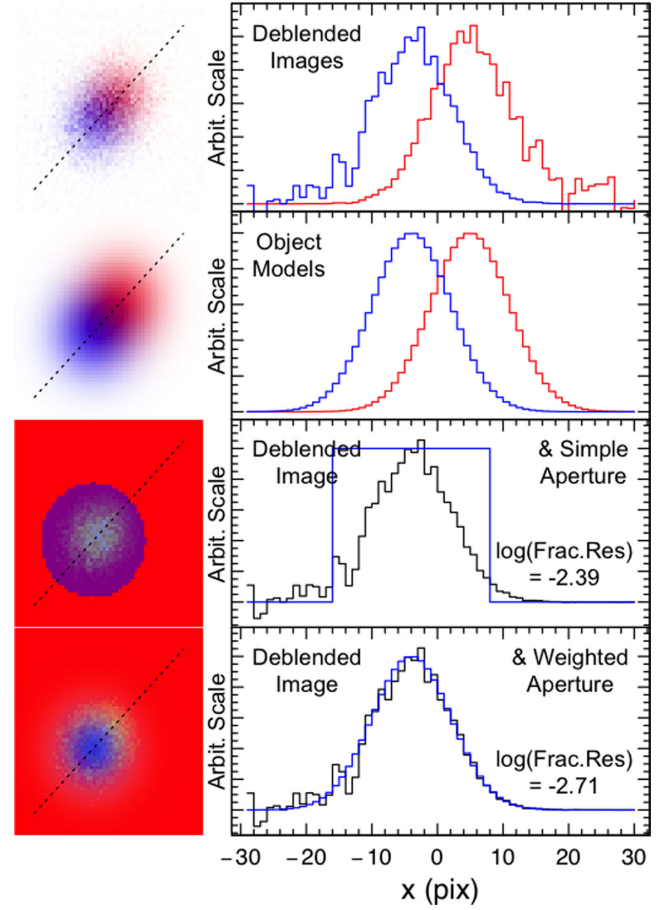
Figure 8. Demonstration of the two different measurement methods, being applied to the simulated objects in Fig. 3. The top panel is the same as the final panel in Fig. 3. The second panel shows models for the two sources. The third panel shows the 'simple' measurement aperture for the blue source (after passing the model through the binary filter detailed in Section 3.7), overlaid on the 'deblended image' ($I(x, y) \times W(x, y)$) in black. The bottom panel shows the 'weighted' measurement aperture, which is identical to the model aperture $M(x, y)$. Again, this aperture is overlaid on the 'deblended image'. In the bottom two panels, the text inset shows the fractional residual between the input flux and the flux measured by the aperture after accounting for aperture normalization (Section 3.8). As is discussed in Section 3.4, in practice the program constructs individual 'deblended apertures' rather than the 'deblended images', shown here, as they are equivalent. We demonstrate deblended images here simply for clarity, to better explain the process.

convolved PSF in the aperture limit). For the maximum correction, the program then measures how much of this flux is missed when measured using the model aperture;

$$C_{max} = \frac{\sum\limits_{x,y} M_i(x, y)}{\sum\limits_{x,y} (M_i^*(x, y) \times M_i(x, y))}. \tag{17}$$

Here $M_i(x, y)$ is the PSF-convolved aperture model, and $M_i^*(x, y)$ is the aperture after possibly going through process of boxcar conversion detailed in Section 3.7.

In addition to this maximum correction, the program returns a second factor, the 'minimum correction'. This factor instead assumes

that the distribution of object flux follows the smallest possible distribution, a PSF:

$$C_{\min} = \frac{\sum\limits_{x,y} P_i(x, y)}{\sum\limits_{x,y} (M_i^*(x, y) \times P_i(x, y))}, \qquad (18)$$

where $P_i(x, y)$ is the PSF function, re-interpolated on to the same pixel grid and centroid as the aperture $M_i^*(x, y)$. This correction factor can be expressed as follows: for every aperture (resolved or otherwise), the minimum correction $C_{\min}$ recovers all flux missed because of aperture weighting or truncation in the limit where the true source is a point source. In this way, the minimum correction can only help the flux determination, by doing the most conservative correction possible. This correction is incorporated automatically into the fluxes output by the program, and both the minimum and maximum corrections are included in the output catalogue.

We note that, when performing PSF-weighted photometry of point sources, because the aperture function $M_i(x, y)$ is equal to the PSF function $P_i(x, y)$, both the minimum and maximum corrections reduce to

$$C_{\min} = \frac{\sum\limits_{x,y} M_i(x, y)}{\sum\limits_{x,y} (M_i(x, y))^2}. \qquad (19)$$

These factors are calculated whenever an empirical PSF or analytic Gaussian FWHM is supplied. It does not require PSF convolution of the aperture to have taken place, which is useful when investigating apertures of standard sizes, such as the 8.25 arcsec radius 'standard apertures' used in *WISE* (Cluver et al. 2014). Note that these factors are defined such that they are multiplicative; that is the final flux is defined as

$$F_{\text{final}} = F_{\text{meas}} \times C_{\min/\max}. \qquad (20)$$

To demonstrate the minimum correction, and its importance, we calculate the factor empirically for a range of simple apertures using the *WISE* W1 G12 PSF, which was derived from observations of Neptune throughout the *WISE* campaign observing the GAMA 12 h field. Fig. 9 shows how the factor (which is an aperture correction,
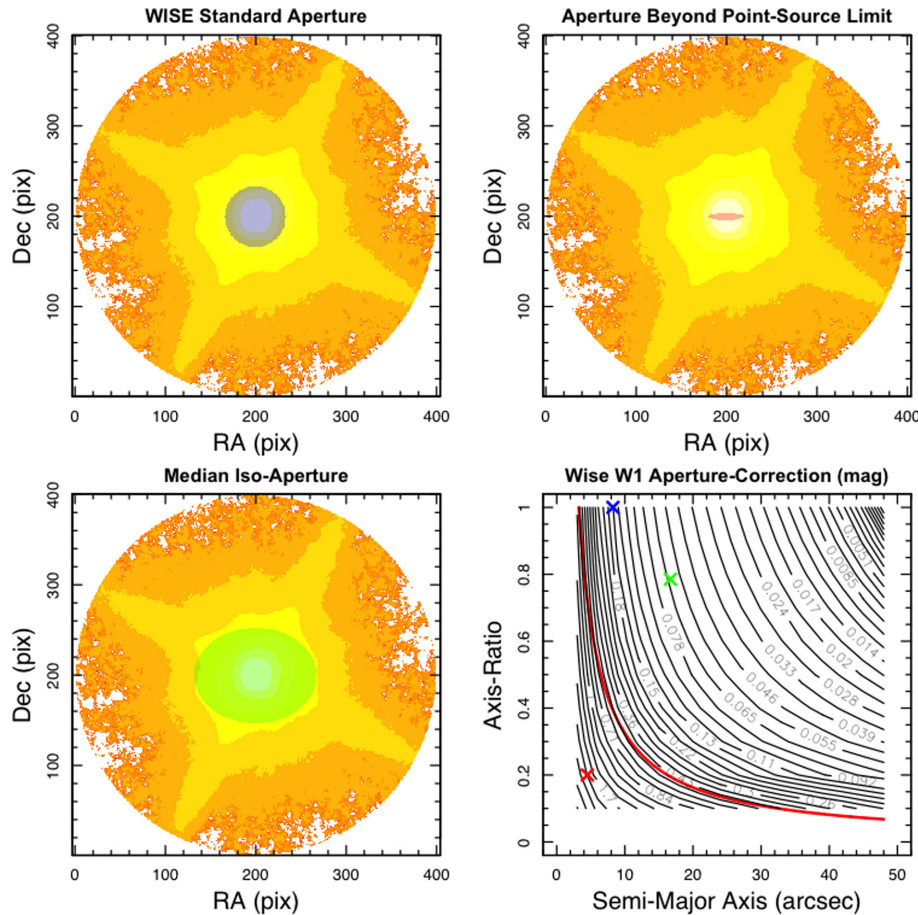
Figure 9. Demonstration of the minimum aperture correction implemented by the program. Here we use the *WISE* W1 G12 PSF, and generate the aperture correction for a range of aperture sizes and ellipticities. Sample apertures were generated at 8000 uniformly distributed points in radius:axis-ratio:position-angle(PA) space. PA was found to have the least impact on variation in the aperture correction, and as such here we show the correction in the radius:axis-ratio space. Three examples of the apertures generated are shown here: panel (a) shows the *WISE* 8.25 arcsec radius 'standard aperture'; panel (b) shows an aperture that is unreasonably small, given the size of the image PSF; and panel (c) shows an aperture with the median semimajor axis length and ellipticity in GAMA. Panel (d) shows the aperture correction value as a function of semimajor axis and axis-ratio, as PA was found to have the smallest impact on the aperture correction. Coloured crosses show value of the corrections for each of the three sample aperture (colours are matched). The solid red line shows the limit where the aperture semiminor axis is equal to half the PSF FWHM; this is an indicator of the minimum sensible aperture that someone might use for measuring fluxes in *WISE*.

because we have simple apertures) varies for a range of aperture sizes and ellipticities. This figure shows that aperture corrections can be substantial (>0.1 mag) when apertures are small ($r_{\mathrm{min}} \leq$ 12 arcsec) and/or highly elliptical ($b/a \leq 0.2$). We note, however, that generating an aperture so small and/or highly elliptical is unlikely (except when intentionally using fixed-size apertures), because the PSF begins to dictate the aperture shape as radius and axis-ratio approach 0.

3.9 Error propagation

Measurements of the various types of uncertainty associated with each flux measurement are generated by the program, such that they can be combined by the user (depending on what they feel is appropriate). While we have detailed the various uncertainties incorporated into each of the various measurements in each Section, here we provide an example of two cases (optical + resolved, and FIR + confused) and how we would derive the uncertainties for measurements in each of these cases.

Internally, the program combines errors as are outlined in this section. That is, the final 'deblended flux error' output by the program will contain, at most, the terms specified here. Other possible error terms are output in the catalogue, but are not combined internally. If the user does not request measurement of one or more of the terms required for this calculation then that/those terms are neglected from the error calculation.

In the optical regime, we typically have high signal-to-noise ratio (SNR), high resolution, and little contamination from blended sources. As a result, the principle sources of uncertainty are typically from pixel-to-pixel noise variations, correlated noise variations, uncertainty in estimation of the sky, and photonic shot noise. As a result, for any typical flux measurement in the optical regime, we would derive an associated uncertainty as follows:

$$\Delta F_i = \left[\sum_{x,y} (D_i \times E_i)^2 + (\sigma_b)^2 \right.$$
$$\left. + \left(\left[1 - \frac{\sum_{x,y} D_i}{\sum_{x,y} M_i} \right] \times \mathcal{D} \right)^2 + \left(\sigma_{\mathrm{bg}} \sum_{x,y} M_i \right)^2 \right]^{1/2}, \quad (21)$$

where E_i is the sigma map associated with the image at the location of the aperture, σ_b is the SD of the sky blanks derived from the randoms/blanks routine, σ_{bg} is the uncertainty of the sky estimate returned from the sky estimate routine (per pixel), and $\mathcal{D}$ is the deblend uncertainty factor given in equation (11). In cases where blanks are not run, but the sky estimate has been calculated, $\sigma_{\mathrm{rms}} \times \sqrt{\sum_{x,y} M_i}$ (i.e. the sky RMS per aperture derived from the sky estimation routine) is used as a proxy for σ_b. The sigma map E_i constrains the uncertainty caused by shot noise, and is defined using some variant of the following equation:

$$E_i(x, y) = \sqrt{\frac{|I_i(x, y)|}{G(x, y)}}, \quad (22)$$

where $G(x, y)$ is the gain per pixel. In cases where a single gain value is supplied, or found in the FITS header, the program uses this value for $G \, \forall (x, y)$. If a weight map is provided, and the program is also provided a single maximum gain value, or one is found in the FITS header, the program will assume that the weight map is inversely proportional to the pixel variance, and will use the gain

value in tandem with the variance map to derive a sigma map with varying gain $G(x, y)$. If the program is provided with a weight map and not a maximum gain value, it will assume that the weight map is identically equal to the inverse pixel variance, and will use this to generate the sigma map. If the program is not provided a weight map or a gain value, then the gain is assumed to be 1 and purely Poissonian uncertainties are derived. Finally, the user may bypass the generation of a sigma map entirely by providing their own as a separate FITS image.

In the FIR regime, where we have confusion of sources, complex and extensive blending of sources, smooth backgrounds, and correlated noise, the major sources of uncertainty are typically pixel-to-pixel noise variations, correlated noise variations, boosting from confusion, and uncertainty in estimation of the sky. However, calculation of the SD of blanks measurements is effective for determination of the RMS uncertainty, the pixel–pixel correlation, instrumental noise, and the contamination from confusing sources. As such, we are able to calculate the FIR uncertainties from the blanks uncertainty, sky estimate uncertainty, and deblend uncertainty alone. These three components none the less account for all the relevant sources of uncertainty in the FIR, identical to those in the optical (with the exception of the shot noise, as this concept ceases being applicable at low photon energies). This consistency of uncertainty determination is particularly useful when performing χ^2 fits to the panchromatic data, as we do not unfairly weight any point over another. This is one of the primary benefits of measuring photometry in this consistent manner.

If the user has an appropriate analytic value for the level of uncertainty in the image introduced by confusion, then this can be specified directly in the parameter file (C, in units ADU pixel^{-1}), instead of having the program perform randoms/blanks. This additional uncertainty term, $\mathcal{C}$, is then calculated using the aperture model, M_i, and the specified confusion per pixel, C, such that

$$\mathcal{C} = C^2 \left[\sum_{x,y} M_i(x, y) \right]^{1/2}. \quad (23)$$

This value is then added in quadrature to the other error terms (in place of the blanks/randoms term).

In all cases, when the program performs any of the various normalization 'corrections' to fluxes (be they provided by the user or measured empirically in the form of the minimum correction in Section 3.8, for example), the program ensures that fractional uncertainty is conserved.

4 TESTING USING SIMULATED SDSS *R*-BAND IMAGERY

Before implementing the program on science images, we first test the code to ensure it is performing as expected. Using synthetic data, we ensure that the code is returning correct photometry by checking for recovery of known input fluxes. As the code has many options that can be activated by the user, testing of all possible permutations of the code's parameter flags was imperative. Here we provide a brief sample of the tests performed on the program, and give examples of the outputs generated by the program with the various options activated. In this way, we hope to demonstrate both the code's functionality and versatility. Additional testing of the various parameters, that is not discussed here, has been performed using the both simulated imaging and real imaging from GAMA. These tests focus mainly on ensuring the correct functionality of each of the programs options, rather than testing the scientific value
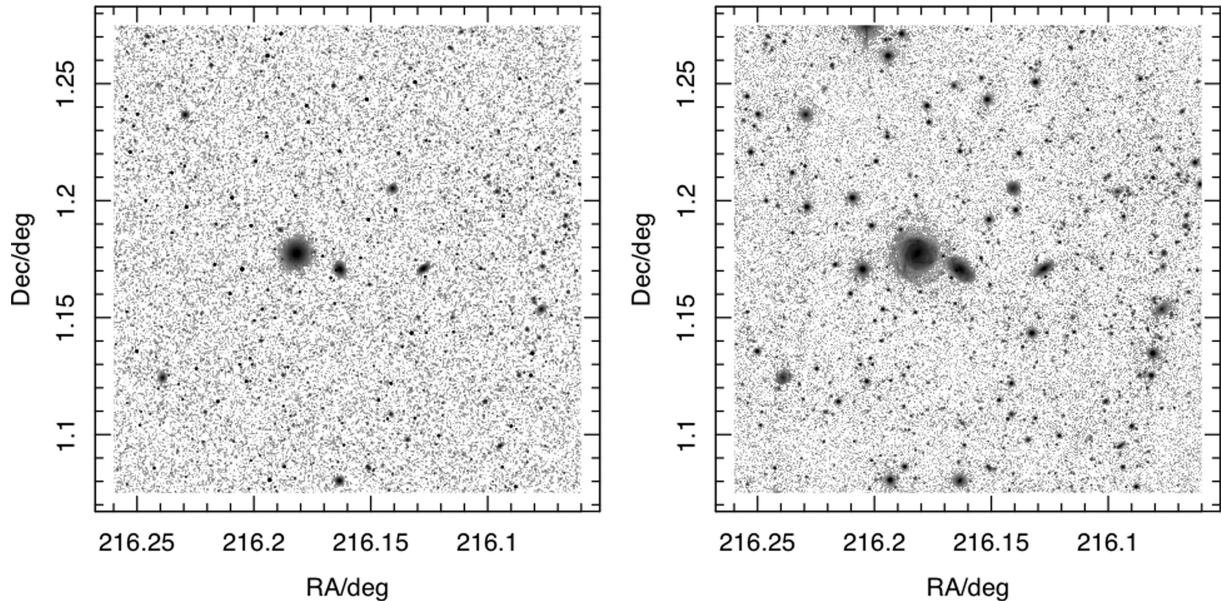
Figure 10. An example of a simulated image (left) created from the GAMA galaxy catalogue and an input SDSS *r*-band image, and the input image that it was based on (right). Galaxies are simulated with exponential profiles, shot noise, and physical backgrounds based on the input image. Images are asinh scaled, with white and black points at 40 and 90 per cent of the cumulative pixel density, respectively.

of each of the settings. As this sort of testing is expected of any program, we do not include discussion of these additional tests here. However, samples of these tests are included in the 'example' sections of the package documentation.

4.1 Generating simulated images

To facilitate further testing of the program, we have incorporated the ability to generate a (optical regime) simulated image into the main body of code. The function is designed to generate a simulated image with galaxy characteristics based on an input catalogue (containing galaxy locations and $2.5 \times$ Kron apertures), an input image (which dictates the dimension of the output simulated image, and also dictates the noise characteristics of the output image), and observation parameters used in calculating photon counts (telescope collecting area, filter effective wavelength and width, exposure time, etc.). Resolved galaxies generated by the simulation function all exhibit perfect exponential profiles, and have simulated fluxes determined by the user's choice of flux-weights. If no flux-weights are provided, galaxies will be scaled to have equal peak-flux. Galaxies are generated via Monte Carlo integration of photon counts simulated for each galaxy's profile and magnitude, up to a ceiling of 10^6 photons per object. Beyond this point, galaxies are generated using analytic exponential profiles. In this way, we naturally incorporate a realistic determination of the per-object shot noise into galaxies whose flux can be influenced appreciably by this effect. Galaxies are convolved with the user defined PSF to emulate observation, and are then added to the image, allowing for simple additive blending of objects.

Random noise is added to the image using $N_{\rm pix}$ random draws from a Gaussian with mean and SD equal to the modal flux and MAD RMS of the input image, respectively. In order to more realistically model true observations, the simulated image can have additional galaxies added such that the galactic number counts follow a power-law model. We use a power law with functional form

$\log_{10} N = 0.38 {\rm m_r} - 4.37$, derived using low redshift object counts from the Millennium Galaxy Catalogue (Liske et al. 2003). By 'padding' the image with low-brightness galaxies we emulate a more realistic sky, as these objects contribute non-negligibly to the noise characteristics of the image. In low-resolution images, this means that we can correctly simulate the existence of confusion noise in our simulation.

Finally, the noise map can be convolved with a user-defined Gaussian, to simulate the process of 'Gaussianization' which introduces correlations in the noise of the data image. This is required if the input image has been previously convolved with a Gaussian, as the measured noise properties in the image (which are used to derive the noise generated in the simulation), will be different before and after Gaussianization. As such, after this optional convolution, the noise properties are again compared to the input image, and are corrected so that they match. The Fig. 10 shows an example of a simulated image created from the GAMA galaxy catalogue and an input SDSS *r*-band image.

Using simulated galaxies, we are able to accurately compare the results of LAMBDAR to our known input flux. Input fluxes are determined from the individual galaxy Monte Carlo integrations, but prior to addition of the sky noise. Thus, we expect the output fluxes to demonstrate the standard 'trumpet' behaviour, as demonstrated in Driver et al. (2011), and shown in Fig. 11. This behaviour arises because, for fixed-distribution random sky noise, a galaxy with lower apparent flux will experience greater perturbation.

4.2 Verification of function behaviour

In addition to simple tests like those already described, we test the behaviour of some of the program's more complicated and/or important functions, which are likely to be run by the typical user. We do this both to test that the program is performing as expected in the general case, and to test the behaviour of the program in exceptional cases.
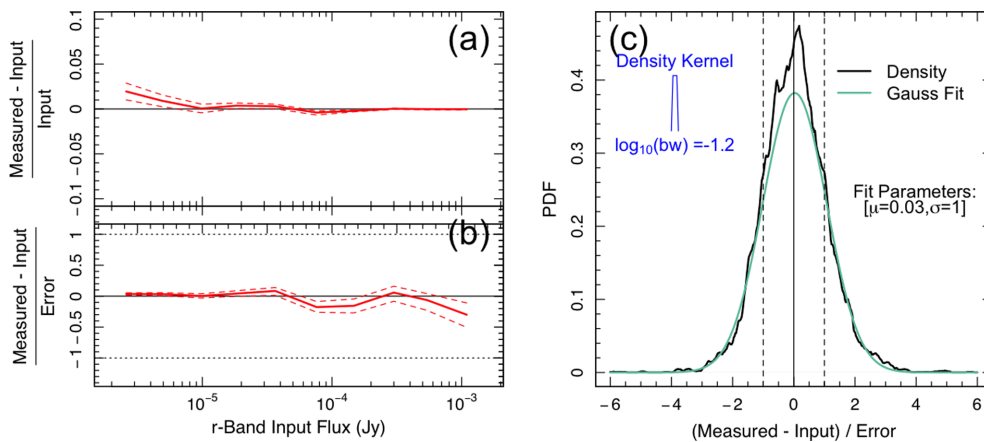
Figure 11. A comparison between the measured photometry (and uncertainties) to input photometry for our SDSS *r*-band simulation. Panel (a) shows the running median (solid red) of the flux residual, with associated error bounds (dashed red), as a function of input flux. Panel (b) shows the distribution of flux residuals divided by the measurement uncertainty; effectively a running median of 'sigma deviation from truth'. Panel (c) shows the kernel density of the sigma deviations. Given appropriate uncertainties (that truly reflect the measurement error), this distribution should be a 0-mean Gaussian with SD of 1. We fit a single component Gaussian to the distribution, and find best-fitting parameters $\mu = 0.03$ and $\sigma = 1.00$. From this figure, we can see that the measured photometry and uncertainties are both a good representation of the input fluxes.
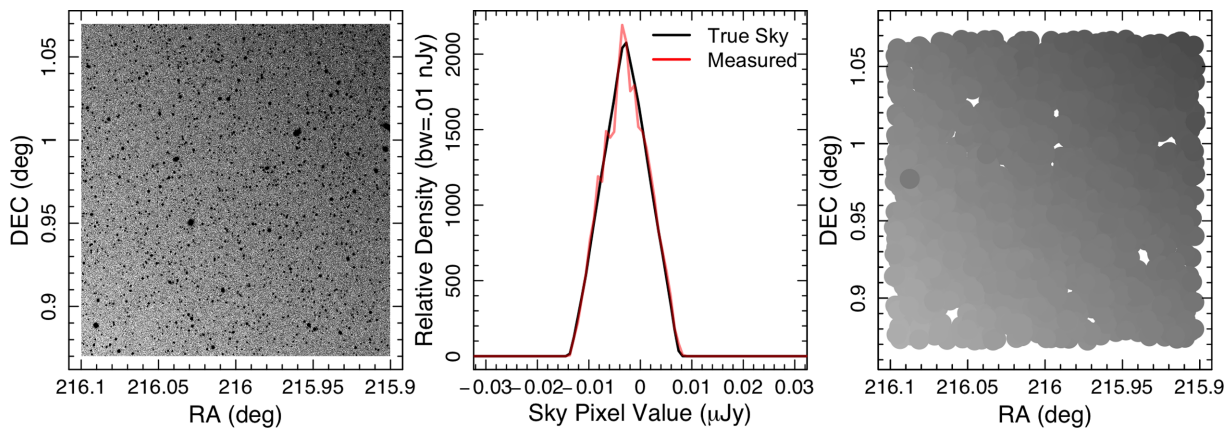
Figure 12. Left: the simulated image with sky gradient. Centre: comparison between the input sky values and the measured sky estimates from the program. Right: the on-sky distribution of estimates, with the same colour scaling as the simulated image (left).

4.2.1 Sky estimation and subtraction

The sky estimate around every galaxy in the input catalogue is determined by fitting concentric annuli around each object and, after optional iterative *n*-sigma-clipping, fitting a running mean and median to each annular bin. This process is able to provide robust sky estimates for each object, while also providing robust uncertainties and parameters that can be used in flagging poor/failed estimates.

As our program determines sky estimates in concentric annuli around each object, we investigate first how the estimate behaves in the regime where the sky value varies strongly on the same scale as the sky estimate annuli. We simulate an astronomical image, as described in Section 4.1, and apply a strongly varying sky of constant RMS. Fig. 12 shows the results of the program's sky estimation in this regime. From this image we can see that the sky estimate behaves well even in this regime, returning estimates that follow the input sky gradient well.

Astronomical images do not always have uniform/constantly varying sky. The most obvious example of this is in the SDSS, where the drift-scan observations lead to sharp boundaries in sky behaviour (in both level and RMS). As such, we test the code's

ability to determine the sky RMS in the regime where we have sharp boundaries in the behaviour of the sky. Fig. 13 shows the results of the program's sky estimation in this regime. We see that the returned RMS values are robust, except at the boundaries of the distributions. At boundaries we see that the returned RMS values tend to lie within the range of the RMS values of the adjacent RMSs, and vary linearly with portion of aperture stamp in each segment.

4.2.2 Object deblends

To demonstrate the behaviour of the program's deblending routine, the program outputs information regarding deblend fractions as a function of iteration. Additionally, the program optionally produces cutouts and CoGs for all/a sample of objects, so that deblend behaviour may be examined by eye. An example of this has been shown already, in Fig. 5. While we do not show any CoGs explicitly for our simulation here, we note that these are none the less output and are an available data product.
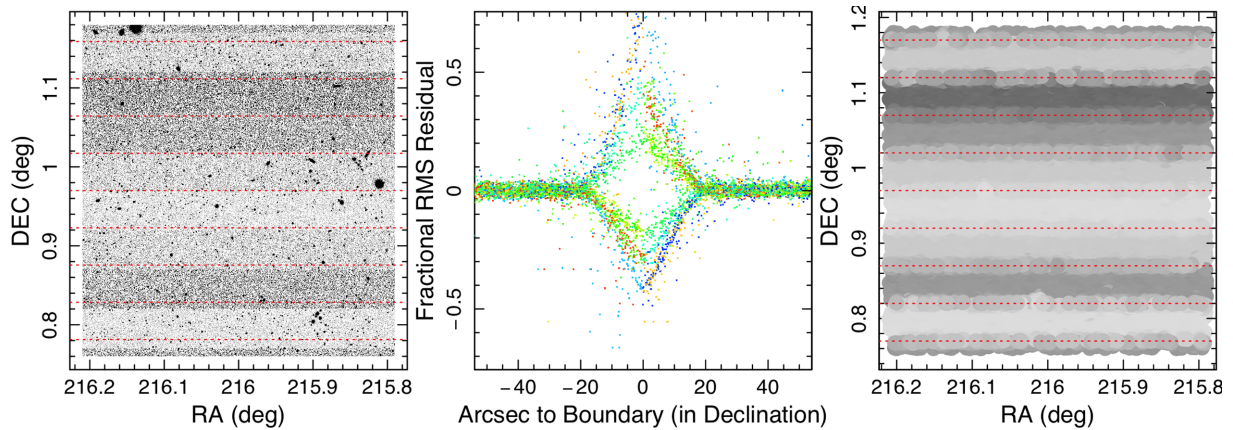
Figure 13. Left: the simulated image with varying sky RMS stripes. Centre: comparison between the input sky RMS values and the measured sky RMS estimates from the program, as a function of distance to the nearest RMS boundary. Points are coloured by declination to demonstrate that divergence from 0 occurs linearly as you approach a boundary, and that the degree of divergence correlates directly with the magnitude of the discontinuity. Right: the on-sky distribution of estimates, where points closer to boundaries are plotted over others (to show boundary effects). Colours in the right-hand panel have been scaled so that the measured RMS value has the equivalent grey-scale to the mean absolute sky value of that sky RMS the simulated image (left). Assuming skies are effectively Gaussian, this allows direct visual comparison of colours in the right- and left-hand panels.

4.3 Flux measurements

We compare the fluxes returned by the program to those input to the simulation. Here we assume perfect source detection, and thus use the known object locations and aperture parameters for our input catalogue. Fig. 11 shows this comparison, and shows good agreement between the input and returned fluxes. As a result, we conclude that the program's flux measurement is being performed correctly.

5 TESTING USING SIMULATED DEEP FIR IMAGERY FROM HERMES

In addition to testing the program using optical simulations, we test the program in the FIR regime using simulated FIR observations of the G10/COSMOS region, described in Wang et al. (2014). The mock imaging utilises the semi-analytic models of Lacey et al. (2015), synthetically observed to mimic observation in the *Herschel* 250 μm filter, using the same observation techniques and integration times as were performed on observations of the G10/COSMOS field by the *Herschel* Multi-tiered Extragalactic Survey (HERMES; Oliver et al. 2012). By using the HERMES mock observations, we are able to test the program's behaviour in the regime where detections are typically lower signal to noise and are more likely to be blended.

5.1 Flux measurements

In order to accurately test our method of measuring FIR photometry in GAMA, we must select the objects for our testing catalogue in the same way that objects are selected in GAMA. That is, we select targets that have either:

(i) an optical apparent magnitude equal to or brighter than $r = 19.8$ mag in the SDSS r band; or
(ii) a SPIRE 250 μm flux $\geq 4\sigma$ above the sky RMS.

Specific details of how the GAMA photometric input catalogues are generated are described in Section 6.2. Briefly, this combined set of objects is required so that we can get measurements for all our targets of interest (i.e. our optically selected sample), and

perform appropriate deblending of sources we can reliably identify as being contaminants not belonging to our target sample. Given our estimate of the 1σ photometric uncertainty from the blanks routine (in Section 5.2) of between 3.39 and 4.47 mJy, we can estimate the 4σ limit of the image as being between AB magnitudes of 13.57 and 13.27. We therefore estimate the 4σ limit as being at an AB magnitude of 13.5, and select all objects in our simulation with input magnitudes brighter than this for our contaminant list definition.

Using this combined catalogue, we measure photometry over 15 iterations with background subtraction and blanks estimation switched on. We then compare the program's measured fluxes (and uncertainties) to the input fluxes. Fig. 14 shows the running median of the fractional flux residual as a function of input flux (panel 'a'), the running median of the sigma deviation from input as a function of input flux (panel 'b'), and the kernel density of sigma deviation from input (panel 'c'). We fit a two-component Gaussian to the distribution to allow fitting of our expected (dominant) population of fluxes around a residual of 0, as well as a population of pathological outliers (caused by contamination from sources not in our contaminant list, both above and below the noise limit). We find that the dominant population is well approximated by a single Gaussian component with mean 0.06 and sigma 0.95. As such, from these figures we can determine that fractional differences between input and measured photometry are prominent (i.e. >10 per cent) only at the fainter end (fluxes <70 mJy) where contaminating flux boosting becomes significant (panel 'a'). However, our uncertainties are appropriate for the sources of error, as our median sigma deviation is constrained to within 0.5σ of 0 for all fluxes brighter than ~10 mJy (panel 'b'). Finally, our measurement errors are not inappropriate over the whole sample, as our distribution of sigma deviation is well represented by a Gaussian with mean ~0 and sigma ~1 (panel 'c'). The secondary component in the sigma deviation distribution demonstrates the frequency of pathological failures, due to flux boosting of faint sources.

5.1.1 Impact of contaminant depth

In Section 5.1, we describe how we define and implement our 'contaminant list' for this FIR simulation. In this simulation, and in GAMA, we choose to define a contaminant list of objects that
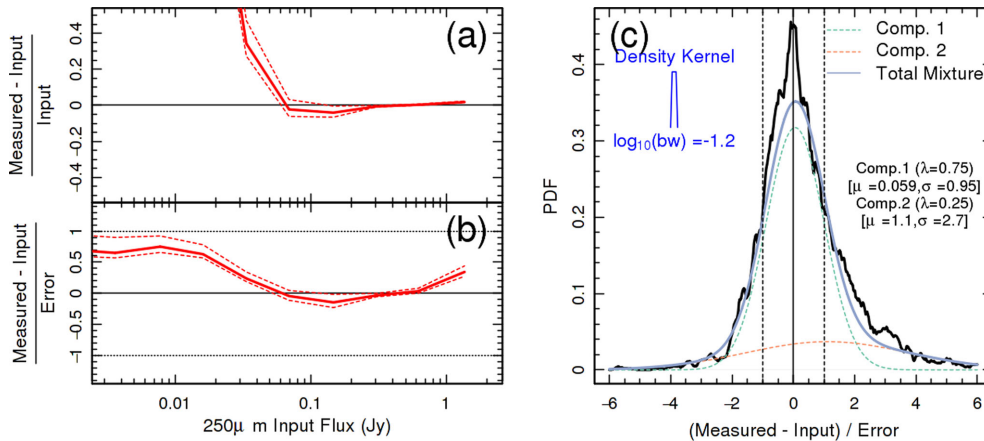
Figure 14. A comparison between the measured photometry (and uncertainties) to input photometry for our HERMES simulation. Panels here are the same as in Fig. 11. Here, however, we fit a two-component Gaussian to the distribution of sigma deviations to allow fitting of our expected (dominant) population of fluxes around a residual of 0, as well as a population of pathological outliers (caused by contamination from sources not in our contaminant list, both above and below the noise limit). We find that the dominant population is well approximated by a single Gaussian component with mean 0.06 and sigma 0.95. From this figure, we can see that the measured photometry and uncertainties are both a good representation of the input fluxes, despite flux boosting of faint sources.

are strongly detected in each frequency range, using conventional source extractors, but which can be reliably distinguished from our optically selected targets. However, this raises the question of what is meant by 'strongly detected', and how fluxes are affected by a change in this definition. In the test above, we implemented a 4σ cut on our contaminant list definition. Fig. 15 demonstrates how flux measurements are impacted by using a contaminant list that is cut at 6σ and 2σ (panels 'a' and 'b', respectively), to demonstrate the impact of the choice of sigma cut. From these figures, we can see that having a contaminant list that is too shallow means that there is a non-negligible increase in flux boosting of faint and bright sources. When using a contaminant list that is much deeper, the fluxes are able to be more reliably deblended but take longer to converge. As a result, in the same number of iterations, there is noticeable shredding of fluxes between sources; seen by the strong dip in the shape of the median distribution, and the negative offset in the mean of the dominant population. This effect will be more pronounced at lower iteration number. Fig. 16 shows the same distributions for the 2σ-cut contaminant list at iteration 0. As iteration 0 deblending is based only on-sky position, fluxes in any pixel are split equally between all sources with equal model coverage at that pixel. The result is clear: faint sources start with too much flux, and bright sources start with too little flux. However, the deeper contaminant list has caused the population of pathological failures to all but disappear.

Internally, the program distinguishes 'science targets' from 'contaminants' using an additional column specified in the input catalogue. The program processes contaminants and targets identically, with the exception that contaminants that are not causally connected to a target are removed from calculation. Similarly, photometry for contaminants is not included in the output catalogue. Causal connection is determined by whether the contaminant's aperture array intersects with a science target's aperture array.

5.2 Verification of randoms/blanks routine

Using the HERMES mock imaging, we can also explore whether the program's internal randoms/blanks routine is able to recover the expected noise and confusion properties of the image. To do

this, we run the program with internal blanks routine activated, and compare the RMS from this function with that measured when we run blank apertures through the program using an externally derived blanks catalogue. In the former case, the program returns a median blanks RMS of 3.87 mJy, with quartile range [3.39, 4.47] mJy. We then compare this value with that determined using the standard method of determining blank apertures. This is done by masking all sources in the catalogue, and generating 1000 random RA and DEC positions in the field. We measure fluxes at each of these locations, and then fit the kernel density of these fluxes (determined using a rectangular kernel of width 0.1 mJy) with a Gaussian to determine the SD. The blanks RMS measured in this way is 3.45 mJy.

6 UPDATING GAMA PHOTOMETRY: COMPARING MEASUREMENTS

For the remainder of this paper, we detail the comparison between the photometry derived from the GAMA PDR and the photometry derived by the LAMBDAR program. With the release of this new data set, dubbed the GAMA LAMBDAR Data Release (LDR), it is the hope of the authors that we will be able to subsequently use this data set for consistent panchromatic analysis of statistically relevant galaxy populations.

The GAMA LDR contains 220 395 sources, fewer than the 221 373 galaxies presented in the GAMA PDR. The difference in source counts is due to a comprehensive process of aperture definition whereby 1706 sources were removed from the catalogue by eye. Simultaneously, 728 sources were created anew, that did not match a previously identified GAMA source.

6.1 Aperture definition

As the program does not perform an independent source detection, it is necessary to define an aperture catalogue for use in this photometric analysis. In the GAMA PDR, apertures in the optical and NIR were generated using a single SEXTRACTOR run over the SDSS *r*-band imagery. Conversely, we use an aperture catalogue that is compiled through a combination of SEXTRACTOR runs
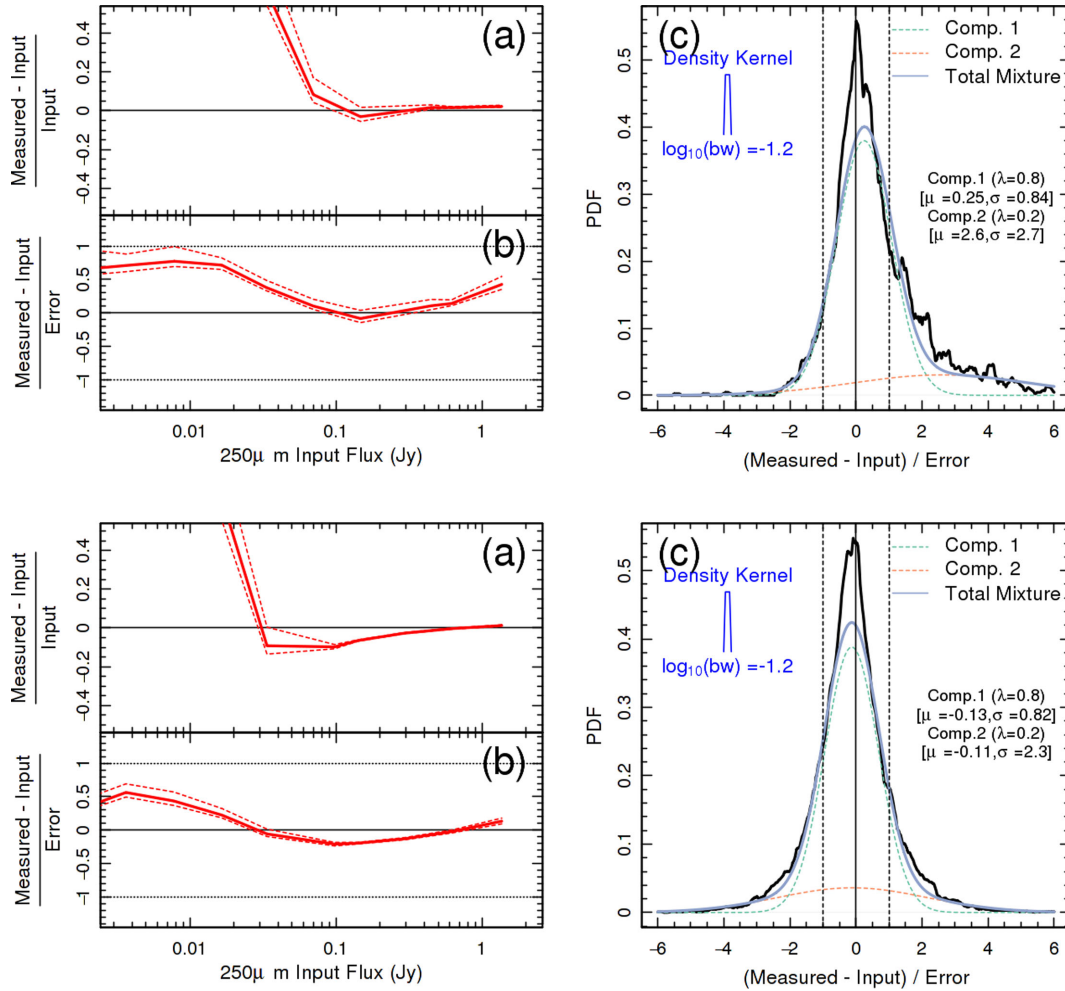
Figure 15. Here we show the same as in Fig. 14, but using contaminant lists cut at 6σ (top) and 2σ (bottom). From this figure, we can see that the choice of contaminant list depth has important effects: a shallow list creates unwanted flux boosting of faint and bright sources, while a deep list slows convergence and increases shredding of sources, as seen by the systematic suppression of fluxes around 0.1 Jy.
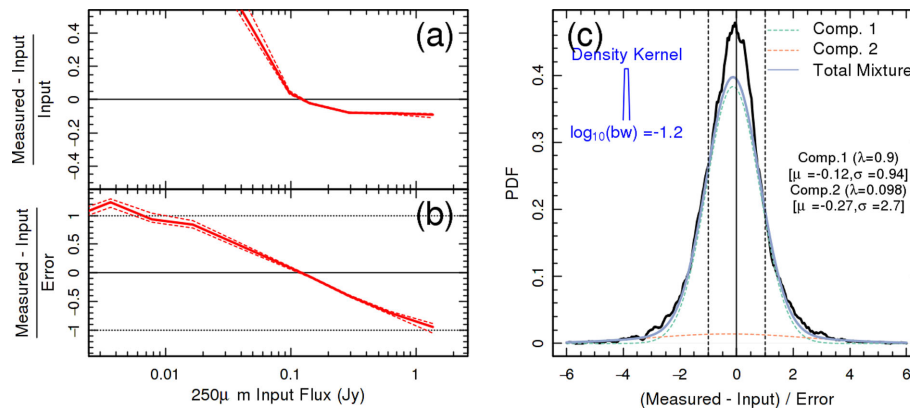
Figure 16. The impact of iterating fluxes, accentuated by examining a case where we have a deep contaminant list, here cut at 2σ. The figure is the same as the bottom section of Fig. 15, except here we show the fluxes as measured at the 0th iteration, where deblending is determined solely by on-sky position. The bias caused is clearly evident in the systematic trend in sigma deviation when plotted against the simulation's input flux.

on SDSS *r*-band imaging, VIKING *Z*-band imaging, and manual aperture creation. This is done because it was apparent that simply running a single SEXTRACTION over the GAMA data was not sufficient to create an aperture catalogue that was robust enough for our purposes.

The aperture definition here follows the following prescription.

(i) Run SEXTRACTOR over SDSS *r*-band, VIKING *Z*-band 'native', and VIKING *Z*-band 'convolved' images.

(ii) Define criteria for determining possibly bad aperture definitions.
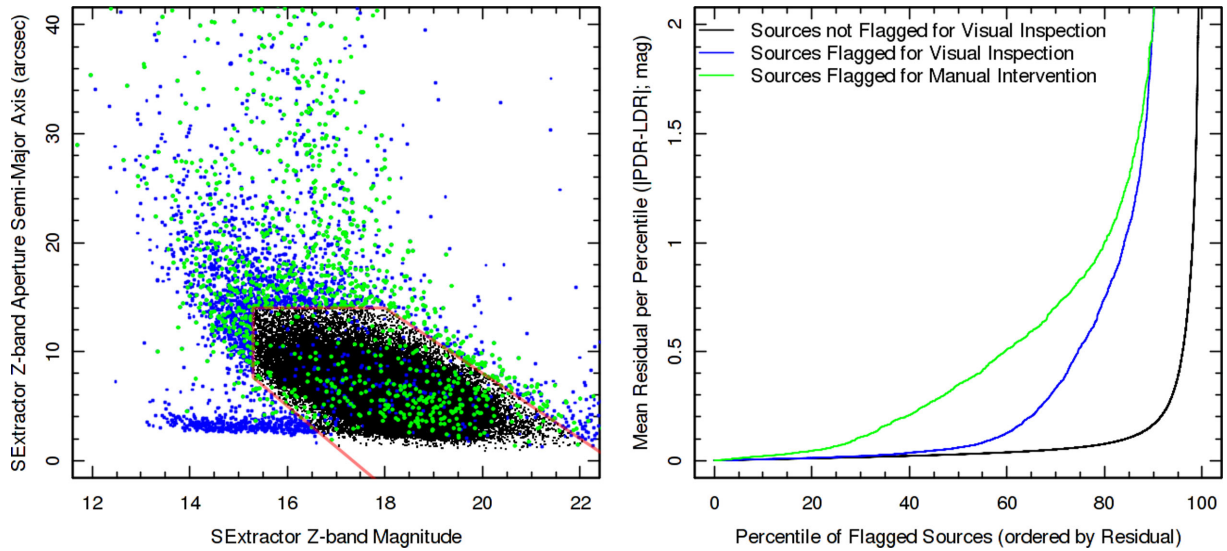
Figure 17. The method of selecting objects with apertures requiring visual inspection. The left-hand panel shows the distribution of GAMA objects in SEXTRACTOR auto magnitude and semimajor axis length, as measured on in the VIKING Z-band, for objects not flagged for visual inspection (black), objects marked for visual inspection (blue), and objects identified (during visual inspection) as requiring manual intervention (green). The selection criteria in surface brightness, magnitude, and size used for determining objects requiring possible manual intervention are shown as red lines; objects outside this boundary are all flagged for visual inspection. Not shown are additional flagging criteria using on-sky position and Z-band coverage (see Section 6.1). The right-hand panel shows the impact of our visual inspection and intervention, quantified by the difference in PDR and LDR *r*-band magnitude. Colours are the same as in the left-hand panel. This figure shows that ∼15 per cent of objects not flagged for visual inspection vary by 0.1 mag or greater between PDR and LDR, whereas ∼40 per cent of objects flagged for visual inspection vary by 0.1 mag or greater. For objects that were identified as requiring manual intervention, more than 70 per cent of objects have magnitude differences of 0.1 or larger.
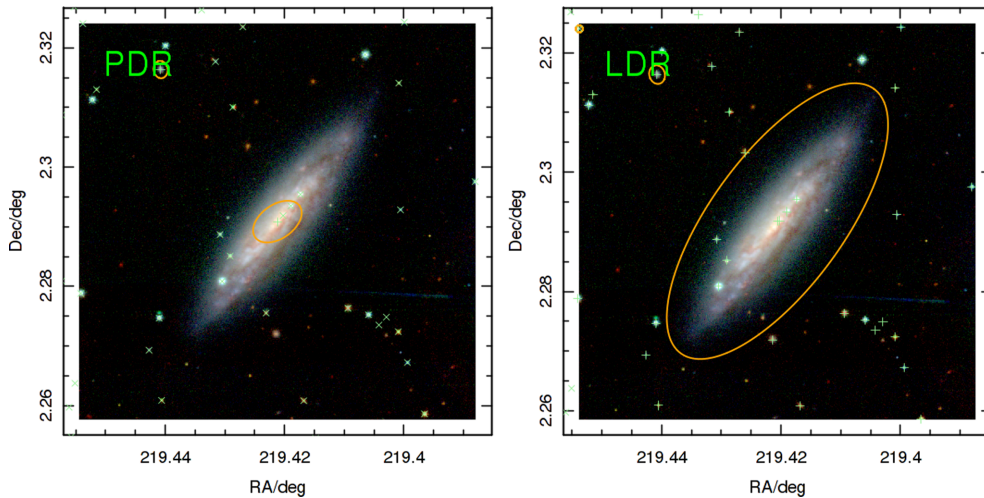
Figure 18. Demonstration of an object whose aperture was flagged for manual intervention (left), and the aperture after correction (right).

(iii) Using a purpose-made visualization tool, re-define problematic apertures.

Here the 'native' and 'convolved' images refer to those at the native seeing and seeing convolved to 2 arcsec, respectively (see Section 2 for more information). For the determining which apertures required visual inspection, we used selection boundaries in size, magnitude, and average surface brightness. Additionally, we include objects for visual inspection that have highly disparate sizes, magnitudes, and on-sky positions, when compared to Sloan. The left-hand panel of Fig. 17 shows an example of the measured sizes and magnitudes of GAMA objects after SEXTRACTION on the VIKING Z-band native images. 4533 objects were flagged for visual inspection (shown in blue), corresponding to ∼2 per cent of all sources.

For visual inspection, 'native' Z-band images were generated with apertures overlaid from each of the SEXTRACTOR runs outlined above. During visual inspection each object is assigned one of these apertures, or (if no aperture is suitable) it is marked for manual intervention. The manual intervention objects are fixed by hand using an online aperture utility, allowing for addition/removal of apertures, and modification of aperture parameters for objects already present in the catalogue. An example of a manually fixed aperture is given in Fig. 18. The object here was originally flagged for visual inspection because of its anomalous surface brightness, and was subsequently marked for manual intervention. Of the 4533 objects flagged for visual inspection, 702 objects were flagged for manual intervention.

The outcome of this process of flagging, visual inspection, and manual intervention, is shown in the right-hand panel of Fig. 17. Here, we show the absolute change in SDSS *r*-band magnitude between PDR and LDR, ranked smallest to largest, for all sources not flagged for visual inspection (black), flagged for visual inspection (blue), and flagged for manual intervention (green). From this figure, we can see that ∼15 per cent of sources not flagged for visual inspection change by more than 0.1 mag between PDR and LDR. For sources flagged for visual inspection, we can see that the fraction of sources that change by more than 0.1 mag jumps to ∼40 per cent. Using the uninspected sample as a baseline (effectively controlling for the difference in method between SExtractor and lambdar), this indicates that our visual inspection has had a substantial impact on the final flux estimates. Further, for sample flagged for manual intervention the fraction increases to more than 70 per cent.

6.2 Catalogues

Having defined the apertures for the science targets, we then must determine what to define as appropriate contaminant lists for analysis in each imaging band. We define three different contaminant lists, which reflects the three broad wavelength regions probed by the GAMA multiwavelength data: the UV-optical-NIR regime (FUV-*Ks*), the MIR regime (*W*1-*W*2), and the FIR regime *W*3-500 µm. We choose these boundaries as they broadly mark the transitions between various contaminating sources; namely disc and halo stars, additional dwarf stars, and high-redshift starburst galaxies, respectively. As a result, the contaminant list required in the optical regime is quite different to that required in the FIR, whereas the MIR and optical contaminants have a substantial overlap. Our contaminant lists are defined here.

In the optical, our contaminant list is defined using the GAMA Input Catalogue v06 (described in Liske et al. 2015), and contains all stellar and galactic objects that do not form part of the GAMA II galaxy sample. In the MIR, we use the sample of all objects that have been identified by the *WISE* team as not matching to a GAMA target as our contaminant list. In the FIR, we use the sample of all objects identified by the H-ATLAS team as those not reliably matching a GAMA target (i.e. with reliability parameter <0.8; see Bourne et al. 2016), as our contaminant list. In each case, we perform a sky-match between the contaminants and science targets, and exclude any contaminants that are within 1 PSF FWHM in the detection band (i.e. *r* band in the optical, *W*1 in the MIR, and 250 µm in the FIR). This is because targets within these limits are likely too close to be reliably detected as contaminating sources. We note that this is not technically the case in the FIR, as spectral slope is a key indicator for the presence of a high-redshift contaminant; however, in practice there are only three contaminants which fall within this limit in the FIR contaminant list. As such we use the method across the board, for consistency.

6.3 Input parameters

For the determination of LDR photometry, we run the program with the settings presented in Table 2. Here we justify our choices of each parameter, as this information will likely inform readers interested in applying the program to other data sets. Parameters not stated in this table are left as default.

We implement a PSF convolution in all bands, including the optical and NIR (where apertures are defined). We do this because there exist point-source objects in the prior catalogue is constructed with future convolution in mind, meaning that point-source objects are given aperture radii of 0.

We perform a local sky estimate in all bands except the *GALEX* FUV. The FUV imaging is Poissonian in nature, as the expected number of sky photons per pixel is less than 1. The sky estimate routine in the program is not designed with Poissonian skies in mind, and it is not clear that the program will behave sensibly in this regime. Fortunately, the FUV imaging has a probabilistic sky estimate incorporated into the imaging (see Andrae 2014 for details). As a result it is not necessary (or sensible) for us to perform our sky estimate on the FUV imaging.

We use PSF-weighted photometry in all images, to improve extraction of fluxes at low signal to noise across the entire wavelength bandpass. We also opt to use recursive descent aperture placement in all but the optical and NIR bands. This is because in the optical and NIR the resolution is so high that apertures will always span a large number of pixels. In these bands we use quaternary aperture placement (done by setting the number of aperture resampling iterations to 0).

Finally, we use pixel-flux-weight weighting in all bands blueward of 12 µm, as the additional weighting can help the program more rapidly converge to the best flux measurement. However, in the shallowest bands (i.e. bands where less than 65 per cent of our target objects are detected at ≥1σ), pixel-flux weighting may act to produce more scatter in the measurements at low iteration numbers, though this is predominantly conjecture. In any case, the choice of inclusion of pixel-flux weighting is largely inconsequential, as we choose to iterate the flux determination, and use a large number of iterations (15).

6.4 Imaging properties

Using the estimated values for the sky (both in value and RMS) from lambdar, we can investigate the properties of the imaging within the GAMA fields. Photometry in the GAMA PDR is measured, per-galaxy, on maps that have already had global backgrounds subtracted (Driver et al. 2016), with the exception of the MIR where photometry has had local backgrounds estimated and subtracted at the time of measurement (Cluver et al. 2014). As the imaging used by lambdar is the same as that used for measuring the PDR photometry (with the exception of the *Herschel* PACS bands; see Section 2), any background that we measure as requiring removal will therefore be present as an unrecognised systematic in the PDR photometry. In Fig. 19 we show a sample of the sky estimates measured by lambdar, both in value and in RMS, as a function of on-sky position. In these images we can see that there exists residual, systematic, variations in the sky level, as well as complex structure in the sky RMS (which is important to consider when deriving flux uncertainties). As these images are used as-is for photometric measurement in the PDR photometry, we conclude that there is likely to exist subtle systematic biases in the PDR measurements and uncertainties. Conversely, as we characterize the imaging properties locally for every source in the LDR, we are able to remove any such biases.

6.5 Flux comparison

Fig. 20 shows trumpet plots for the *GALEX* NUV, SDSS *r*, VIKING *K*, *WISE* *W*1, and PACS 160 µm bands. A full compilation of trumpet plots in all bands can be found in Appendix C. From these figures, we can see that the photometry from lambdar agrees broadly with the photometry presented in the PDR, however there are indeed
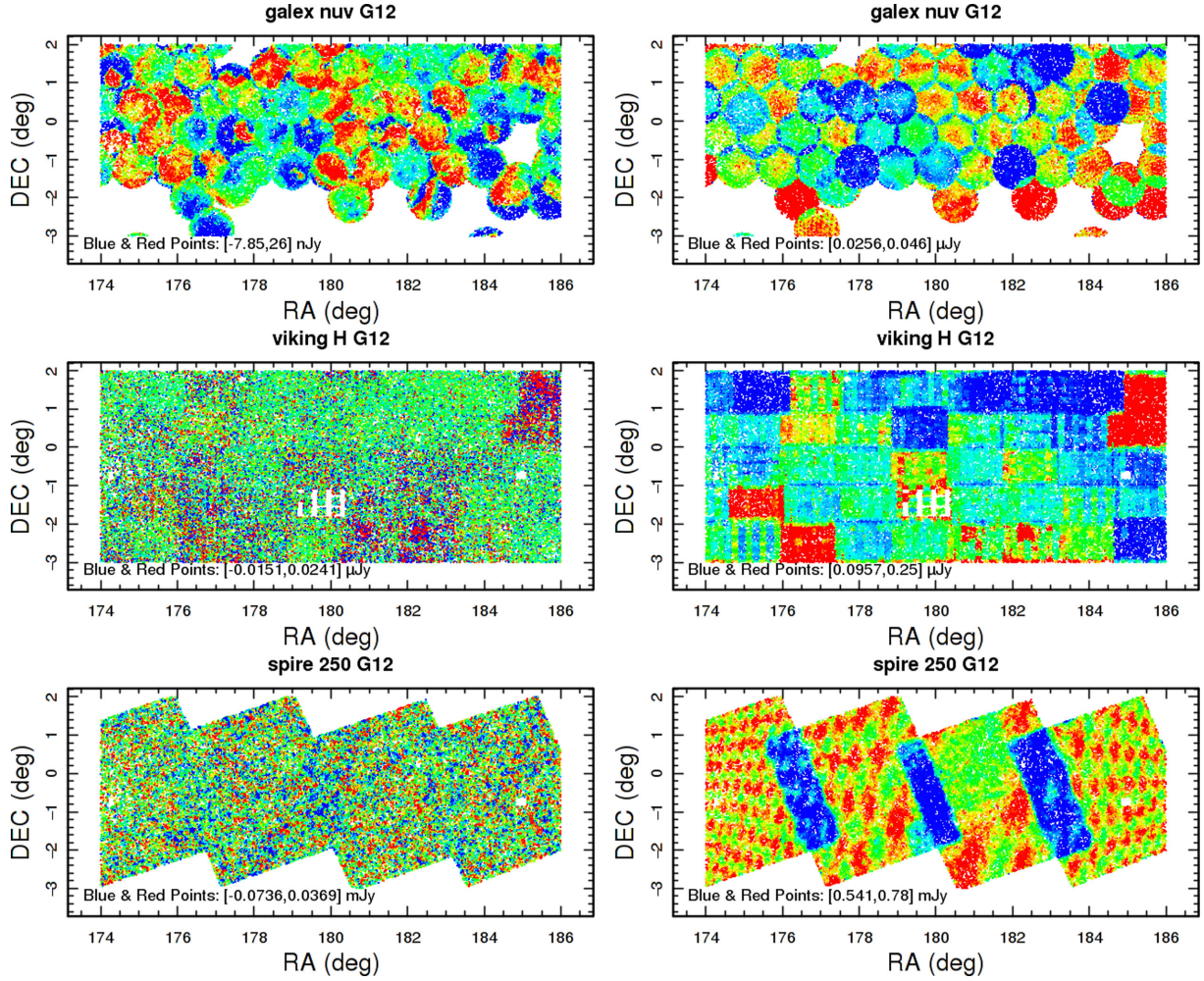
Figure 19. A sample of the on-sky distributions of local sky estimate (left) and local sky RMS (right) for three bands in the G12 field. The top row is the *GALEX* NUV, the middle row is the VIKING *h* band, and the bottom row is the SPIRE 250 μm band. In each image, the points are scaled with blue and red points at the 10 and 90 per cent values, respectively. The absolute values corresponding to these blue and red points are given in the bottom left of each figure. As these filters have all been sky-subtracted prior to running LAMBDAR, any variations seen in the left-hand column represents flux that will contribute adversely to the final measurement if not removed. Similarly, complex variation in the sky RMS in the right-hand column must be recognized for appropriate uncertainty estimation. We note that the pattern seen in the H-ATLAS mosaic sky RMS (bottom right) is a Moiré pattern induced when the mosaic was resampled on to the standard GAMA field centre (see Driver et al. 2016), and is not present in the original H-ATLAS imaging.

variations in the distributions that cannot be explained on signal-to-noise grounds. For example, the structure in the *WISE* trumpet is likely a combination of many effects, but is overarchingly due to the differences in apertures (fixed size versus variable), and deblending (none versus some). The difference in fixed and variable aperture sizes can be seen in the systematic trend whereby LDR fluxes are fainter for faint PDR fluxes, and brighter for bright PDR fluxes. This is because brighter objects are also typically larger, and a fixed size aperture will systematically miss flux. Similarly, faint sources are typically small, and are much more sensitive to being contaminated by neighbouring sources. As a result deblending creates an increased scatter downward (which is larger at the faint end of the distribution) as fixed-size apertures with no deblending allow flux to be double counted, whereas this is not possible in LAMBDAR's deblending.

In addition to showing the agreement between the measurements made in the PDR and LDR data sets, we also demonstrate the utility of matched aperture photometry in terms of number of flux estimates. Fig. 21 shows the number of measurements made in the

LDR and PDR data sets per band. In addition, the figure shows the fractional coverage of each band. From this figure, the utility of matched aperture photometry is quite apparent; the LDR data set has performed a measurement for every object in every band for which there exists coverage, while the PDR has a substantial number of missing flux estimates in some bands (particularly the UV and MIR), as no measurement was made. Furthermore, we can see the gain in positively detected sources (i.e. signal to noise greater than 1) in the LDR data set, over the often signal-to-noise limited PDR data set.

In the FIR trumpet plots, seen in Appendix C, there are two particular differences that are of note. First, there exists a population of objects with large magnitude offsets (>0.5 mag) at moderately bright PDR magnitudes (clearest in SPIRE 250 μm), which cannot be explained as variations due to backgrounds/noise. Inspection of these objects shows that they are all objects that have been deblended from a high-redshift contaminating source (see the contaminant list definition in Section 6.2). This can be seen in Fig. 22, where we show the residuals between LDR and PDR fluxes, coloured by
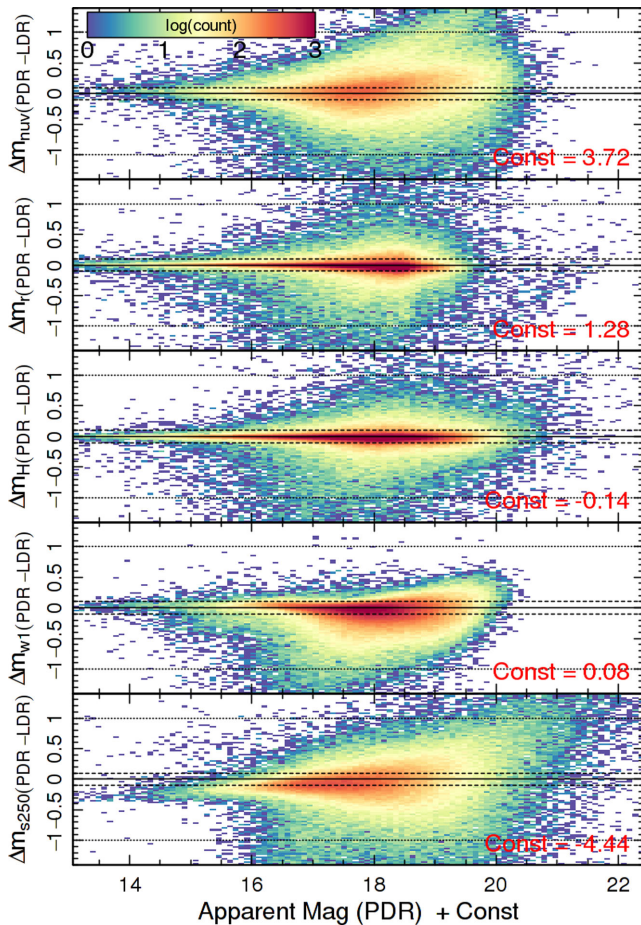
Figure 20. 'Trumpet' plots showing difference in magnitude versus PDR magnitude for the *GALEX* NUV, SDSS *r*, VIKING *H*, *WISE W*1, and SPIRE 250 µm bands, demonstrating that the photometry is in broad agreement with the PDR photometry, but none the less shows systemic differences caused by subtle differences in measurement methods. Each panel has a horizontal offset applied, which is given in the lower right of each panel. Horizontal dashed and dotted lines are shown at ±0.1 and 1 mag, respectively, for reference.
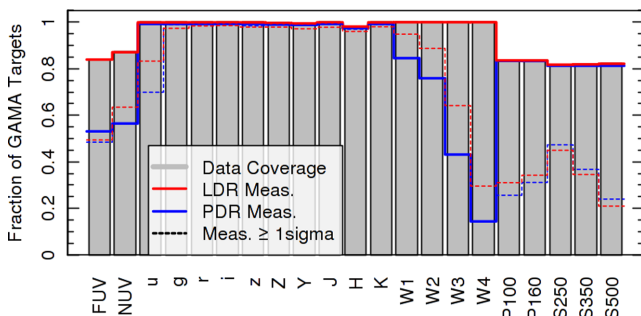
Figure 21. The number of measurements made, per band, in each of the LDR (red) and PDR (blue) data sets. The fractional coverage of each band is shown as the grey vertical bars. The benefit of performing matched aperture photometry is apparent; for each optically measured object (i.e. 100 per cent of GAMA targets), there exists a measurement in every band where there exists coverage. Conversely, the PDR data set shows large numbers of missing measurements where data exists in some bands (the UV and MIR particularly). Further, we show the fraction of all sources that are detected at 1σ or greater as dashed lines, for both the PDR and LDR. As the PDR photometry are signal-to-noise limited in the *GALEX* NUV and *WISE* MIR, the solid and dashed blue line in these bands overlap.
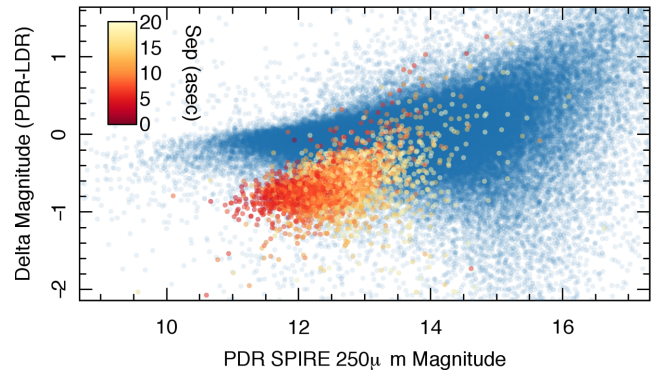
Figure 22. Demonstration that the population of objects offset from 0 in the SPIRE 250 µm trumpet is caused by deblending of nearby contaminants. Here colouring is by separation between the object and its nearest-neighbour contaminant, in arcseconds. The blue points in the background is the distribution of all objects not matched to a contaminant within 20 arcsec, for reference.

separation to the nearest high-z contaminant. From this figure, we can see that the offset in the residuals changes systematically with distance to the nearest contaminant. The systematic trend with separation, and the fact that the cloud is dispersed around a value of $f_{\mathrm{LDR}}/f_{\mathrm{PDR}} \sim 0.5$, suggests that these are objects for which LAMBDAR has deblended a contaminant that was not subtracted in the PDR. In the final trumpet plots in the appendix, this population is far more heavily dispersed than in Fig. 22.

Secondly, the brightest FIR objects are systematically dimmer in the LDR data set than in the PDR. This is because the Bourne et al. (2012) program implemented our maximum normalization factor by default, rather than the minimum factor automatically employed in LAMBDAR. As the brightest fluxes typically belong to the objects with the largest apertures, the difference in normalization factor becomes even more pronounced. Using our maximum factor, LAMBDAR recovers well the fluxes in the PDR at the bright and faint ends; however, we opt to report our fluxes as calculated using the minimum correction as it makes fewer implicit assumptions about the distribution of source flux (see Section 3.8).

6.6 Error comparison

We compare the uncertainties measured by LAMBDAR compared to those given in the GAMA PDR. Fig. 23 shows a comparison between the uncertainties measured for a range of bands (split into individual components), compared to the uncertainties present in the PDR release. A full compilation of error distributions can be found in Appendix C. From these figures we can see that, while there exist differences in the error components in some bands, LAMBDAR is typically returning uncertainties that are consistent with what was previously determined. Furthermore, we can be confident that the uncertainties used in all the different bands are determined in a consistent manner, giving us confidence that differences in uncertainties between PDR and LDR are real and likely due to differences in, for example, measurement methods. This fact will ensure that we are not biased during SED fitting because of uncertainties in one or more bands being systemically under/overestimated when compared to those in adjacent bands.
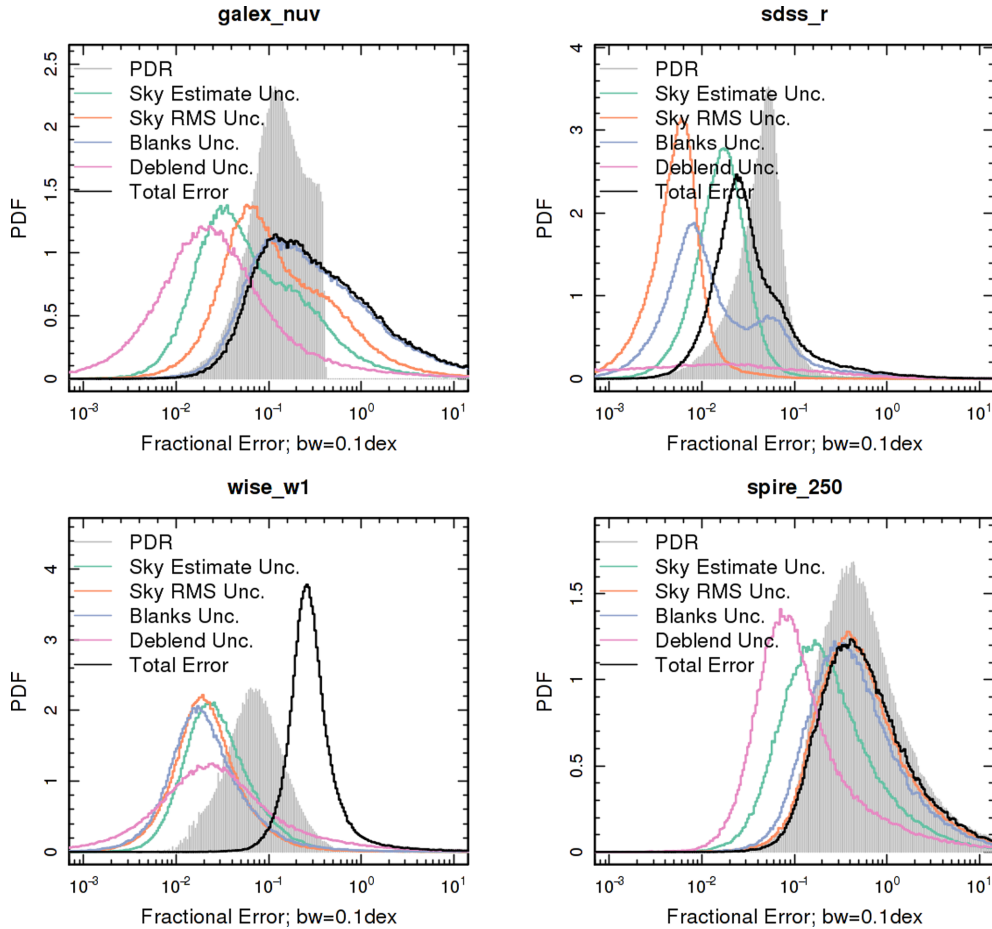
Figure 23. Comparison of the uncertainties returned by the program, split into various components (coloured lines), compared to those in the GAMA PDR (grey histogram). We note that typically our fractional uncertainties are consistent with those measured previously. This is not true in all bands, with the SDSS *z*-band being a stand-out above with a factor of ∼2 difference between the PDR and LDR final uncertainties. This is not necessarily unexpected, given that the measurement methods used in the PDR and LDR data sets are different, the apertures are different, the factors incorporated into the uncertainties are different, and the methods of determining those factors are different. However, we can now be confident that the uncertainties are determined in a consistent manner, and are therefore not going to create biases in multiband SED analyses.

6.7 Colour comparison

Fig. 24 shows colour distributions for a sample of five colours in the 21-band PDR and LDR data sets. Again, a full compilation of colours can be found in Appendix C. From these distributions, we can determine two particular parameters of interest: the effective width of the distribution, and the distribution outlier fraction.

The effective width of the colour histograms is informative as, assuming there exists some fundamental distribution of galactic colours, any measured distribution will trace the fundamental distribution convolved with a Gaussian distribution (reflecting the combined measurement uncertainties for each galaxy). As a result, the distribution that is measured to have a smaller effective width is therefore that with smaller measurement uncertainty. Due to the highly non-Gaussian shape of the colour distributions, we use the width of the central 80 per cent of the distribution (i.e. the number of magnitude separating the 10 and 90 per cent limits) as our effective width. The 10 and 90 per cent limits of the colour distributions are shown graphically in Fig. 24 as a horizontal bar, coloured for each distribution. Furthermore, Fig. 25 shows the measured effective widths for every adjacent colour in GAMA. The figure shows that the LDR colours are equivalent to (within the 0.01 mag density bandwidth), or narrower than, the PDR colours across the entire

data set, with the exceptions of the FUV-NUV, *W*2-*W*3, and *W*3-*W*4 colours. We note that these three colours correlate with the bands containing the strongest sigma-cuts in the PDR data (see Fig. 21), meaning that the distribution of colours will likely be artificially narrow due to matching bias; objects with fluxes below the sigma limit of the catalogue are incorrectly matched to contaminating objects with fluxes above the sigma limit. This effect is prominent when matching data that has been heavily sigma-cut to data of greater depth, and is exacerbated when the sigma-cut data traces a fundamentally different range of populations to the deeper data, as is the case in the GAMA UV and MIR data. As the effect only works in one direction (i.e. low-sigma source fluxes are replaced by high-sigma contaminant fluxes, but never vice versa), the result on the colour distribution is the removal of noisy measurements, and replacement with strong detections. Given this effect, and assuming that the colour distribution of contaminating sources lies within the limits of the distribution of target colours, the effect will cause a reduction in the effective width of the colour distribution when compared with the unbiased distribution. We note that this effect can only occur when comparing photometry where one data set has been modelled (as in the case of SDSS model magnitudes) rather than measured directly, or where one data set is subject to
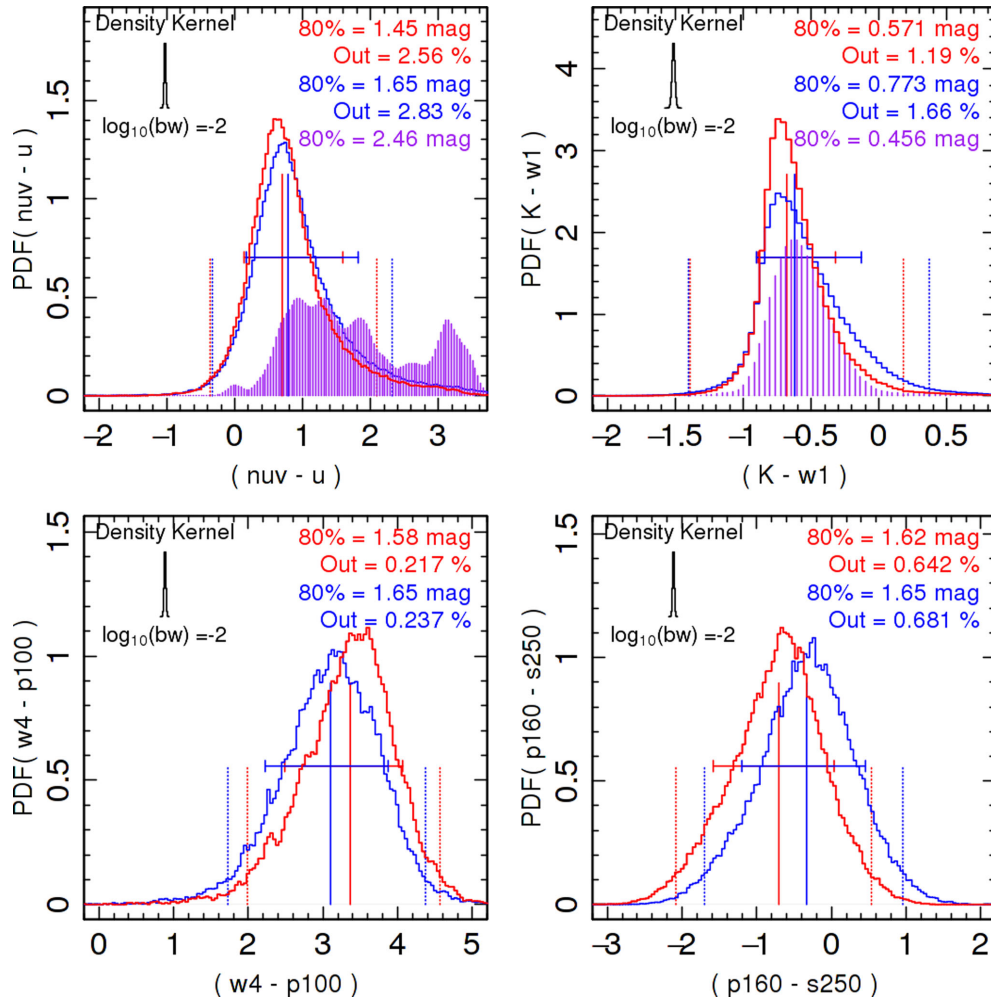
Figure 24. Colour distributions comparing PDR (blue) and LDR (red) photometry for the *GALEX* NUV – SDSS *u*, VIKING *K* – *WISE W*1, *WISE W*4 – PACS 100, and PACS 160 – SPIRE 250 bands. These bands are selected for demonstration as they are colours which cross facility boundaries, meaning that PDR photometry in these colours may be systematically inconsistent. In the first two panels, the purple histogram shows the colours of galaxies that form the templates of Brown et al. (2014). Inset text shows the effective colour width at 80 per cent, and the outlier rate, for each distribution. The inset graph shows the density kernel used in calculating the PDFs. Samples here are matched so that only objects that are detected at (at least) 1σ in both bands, in both photometry samples, are present. This is done to remove complicated selection effects and objects with spurious colours. PDFs here are generated using a kernel density estimator, with kernel as shown in the upper right of each panel.

strong signal-to-noise selection. As this is not the case in the LDR photometric data set, this cannot explain the reduction in scatter that we see in each of our colour distributions.

The outlier fraction is similarly informative as it details the number of catastrophic outliers in the colour distribution. We define the outlier fraction as the percentage of objects that are more than 0.5 dex beyond the 10 and 90 per cent limits of the colour distribution. These points are shown graphically in Fig. 24 as vertical dotted lines coloured for each distribution. Furthermore, we show the outlier fraction measured for every adjacent colour in GAMA in Fig. 25. The figure shows that the number of outliers is lower in each of the LDR colour distributions compared to the PDR distributions, again with the exception of the *W*3-*W*4 colour (for the same reason as above). We also see a modest increase in outlier fraction in the internal SPIRE colours. As the methods for determining photometry in SPIRE are similar in the LDR and PDR data sets, this increase can likely be attributed to differences in the choice of contaminant list. This is because the method is known to be similar, and the colour distributions themselves are of equal width (indicating that the ma-

jority of sources are in agreement). A detailed comparison of LDR photometry with individually tailored PACS and SPIRE photometry is provided in Valiante et al. (2016). Most importantly, we note that the outlier fractions at the boundaries between facilities (shown as vertical dotted lines) in the LDR are consistently lower than or equal to the PDR, demonstrating that the consistent measurement of photometry is having a major impact in these colours.

Finally, it is particularly interesting to examine what new parameter space is opened for analysis when performing this sort of consistent matched aperture photometry, compared to what was available previously in the PDR. Specifically, the far greater depth of measurement in the MIR allows us to explore the highly important polycyclic aromatic hydrocarbon emission, which traces (among other things) the hot emission from dust surrounding stellar nurseries. By probing to lower fluxes, we open up a greater parameter space for investigation in this region. We demonstrate this in Fig. 26, where the additional measurements made by LAMBDAR have pushed out down and left in the parameter space shown. We note that this increase in parameter space cannot be explained by adding
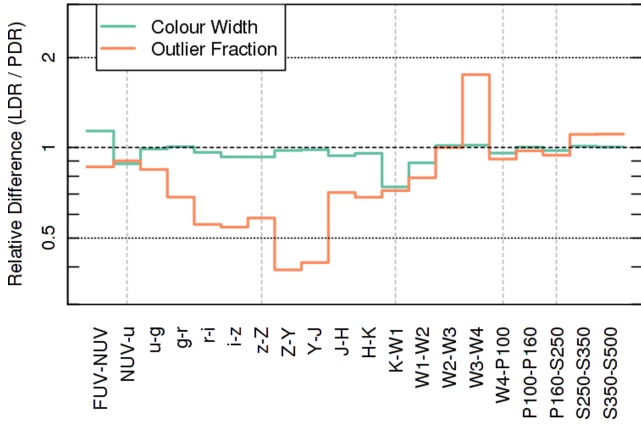
Figure 25. Relative changes in the width (cyan) and outlier fraction (orange) of the colour distributions for adjacent bands in the PDR and LDR. Facility boundaries, where the colour shown uses fluxes from different instruments (and therefore typically different measurement methods), are marked on the figure by grey vertical dotted lines. We can see that the colour distributions in the LDR data set are narrower than the PDR data set, with the exceptions of the FUV-NUV, $W2$-$W3$, and $W3$-$W4$ colours. Similarly, we see an improvement in the outlier fraction for all colours, with the exceptions of the $W3$-$W4$ and internal SPIRE colours. We note, in particular, that improvements in the colour distribution widths are greatest (compared to adjacent colours) when crossing facility boundaries; i.e. where measurement methods in the PDR change. Similar improvements in outlier fraction are seen at these boundaries also. This indicates that the consistent measurement is having a large improvement in these bands, compared to the PDR. The dotted lines mark where the ratio is different by a factor of 2, in denominator and numerator. Possible explanations for these differences seen in the FUV-NUV, $W2$-$W3$, and $W3$-$W4$, are described in the text. Comparison of photometry in PACS and SPIRE is presented in Valiante et al. (2016).
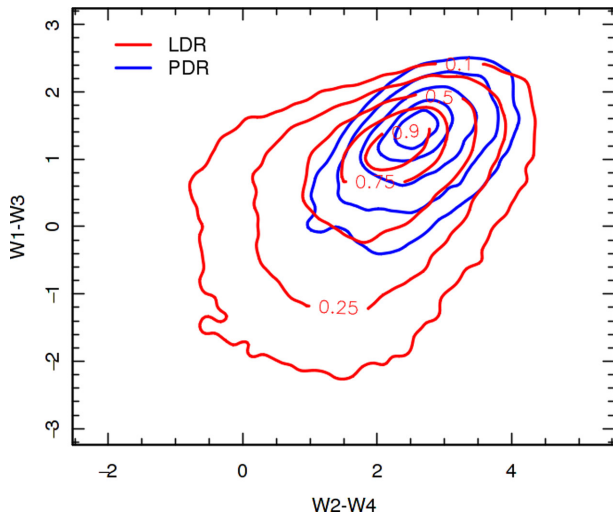
Figure 26. Demonstration of the increased range of spectral colours that are able to be probed when performing matched aperture photometry, as bias against weak emission is removed. Here we show how, in the MIR, an increase in the catalogue depth allows us to push further into the colour–colour space, when compared to the sigma-clipped measurements previously available. Contours are numbered by the fraction of sources outside the contour. The blue contours show the distribution of PDR colours, while the red contours show the full distribution of LDR colours. As the MIR data are useful for object classifications (see e.g. fig. 5 of Cluver et al. 2014), we can determine that this expanded parameter space is populated primarily by a range of morphological types, from high-mass, low star formation rate ellipticals, to low-mass, moderately star-forming disc systems.

additional scatter to an additional sample of detections drawn from the same distribution as that in the PDR, as this effect would cause a uniform broadening in all directions. In contrast, what we see is a distinct increase in parameter space in two directions, while the other two colour boundaries remain well defined.

6.8 The final product

We began this paper with a demonstration of an object whose photometry was inconsistent across the full GAMA bandpass. It would be remiss to not then demonstrate at the conclusion of the paper that this process had not, at the very least, been successful in producing consistent panchromatic photometry in this case. As such, Fig. 27 shows the photometry for this object, as measured by LAMBDAR, with a fit performed by the energy-balance code MAGPHYS (Da Cunha et al. 2008; Da Cunha & Charlot 2011). We see that MAGPHYS has been able to produce a better fit to the panchromatic SED, indicating that LAMBDAR has produced photometry (and uncertainties) that are more consistent across the entire bandpass, and thus the SED fit is now a much more reliable representation of the object's true panchromatic emission.

Comparing the fits from PDR and LDR, we find that the LDR SED is a better fit to the data $\chi^2_{\rm best} = 11.69 \rightarrow 2.11$. Taking each of the output parameters (with indicated 1σ intervals) entirely at face value, the LDR SED shows an older system $t_{\rm form}({\rm Gyr}) = 9.997 \pm NA \rightarrow 9.182^{+0.135}_{-0.000}$, but whose mass-weighted and luminosity-weighted ages are both younger $age_m({\rm Gyr}) = 9.80 \pm NA \rightarrow 8.79^{+0.29}_{-0.00}$ and $age_r({\rm Gyr}) = 9.45 \pm NA \rightarrow 8.85^{+0.30}_{-0.00}$. The SED is dustier $\log_{10}(M_D/{\rm M}_\odot) = 6.81 \pm NA \rightarrow 7.10^{+0.09}_{-0.03}$, but has maintained an equivalent stellar mass $\log_{10}(M_*/{\rm M}_\odot) = 9.507 \pm NA \rightarrow 9.417^{+0.115}_{-0.005}$. Bursts of star formation have been less recent $t_{\rm lastburst}({\rm Gyr}) = 8.00 \pm NA \rightarrow 8.473^{+0.88}_{-0.00}$, but the overall star formation has been more sustained, as shown by a lower star formation time-scale $\gamma({\rm Gyr}^{-1}) = 0.28 \pm NA \rightarrow 0.14^{+0.00}_{-0.00}$ which determines the overall star formation rate as a function of time ${\rm SFR}(t) \propto e^{-\gamma t}$ (neglecting bursts). Note that the 1σ uncertainties on the PDR SED parameters are uniformly $\pm NA$; these have not been forgotten, but rather are all not calculable. This is because the fit has been forced into an area of parameter space where there is limited modelling, meaning that the PDF effectively becomes delta-function-like. In contrast, the LDR SED provides errors that are typically bound within an non-zero interval on one or both sides.

Full SED analysis of all galaxies in GAMA is left for an upcoming publication.

7 UPDATING GAMA PHOTOMETRY: COMPARING DERIVED PROPERTIES

In addition to examining the change in the flux of measured sources, we also investigate how the new photometry impacts the measurement of some particular properties of interest. Specifically, we examine how the photometry impacts the measurement of stellar masses, star formation rates, and the stellar mass to star formation rate relation.

To begin, we estimate the stellar mass of every galaxy by fitting SEDs across the optical and NIR bands, as described in Taylor et al. (2011), for both the PDR and LAMBDAR photometry. The median residual between the stellar masses for the two data sets is -0.004 ± 0.030 dex, which is both consistent with no difference and much lower than the median uncertainty of both data sets, which is 0.108 and 0.111 for the PDR and LDR masses, respectively. This is not surprising given the consistency in colours and fluxes across
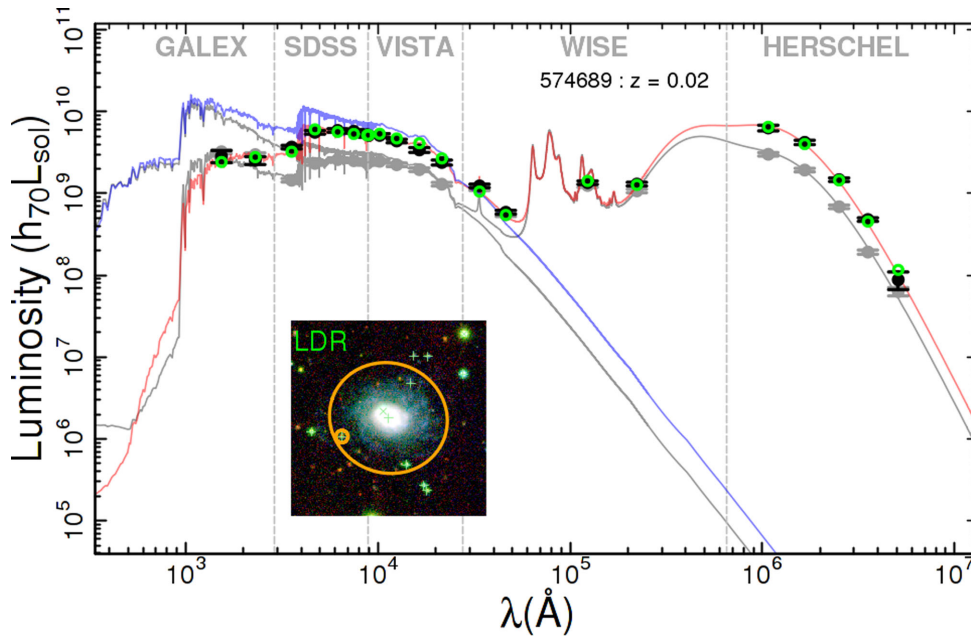
Figure 27. The panchromatic SEDs of GAMA object G574689. The grey SED is as determined when using photometry from the PDR catalogue (i.e. the same as Fig. 1), while the coloured lines show the SED fit to photometry returned by LAMBDAR. Note that after our procedure, the aperture used for all bands is consistent (shown in the inset image) and the photometry is therefore also consistent. Here the LDR photometry is in black, model photometry is in green, unobscured SED is in blue, and the obscured SED is in red. As with Fig. 1, the inset is an RGB cutout using the VIKING *H* – SDSS *i* – SDSS *g* bands.

the optical and NIR bands, which are used to estimate the stellar masses here.

Utilizing the MIR and FIR data, we can estimate a star formation rate using physically motivated predictors. As a demonstration, we examine predictors using both the *WISE W4* and *Herschel* PACS 100 μm band, for both the LDR and PDR data set. We use luminosity-based SFR indicators for the *W4* and 100 μm bands, with the 100 μm indicator coming directly from Davies et al. (2016), and the *W4* indicator being derived in the same way. Having determined stellar masses and SFR estimates for both the LDR and PDR data sets, we can investigate how well the two data sets are able to recover the main sequence of star-forming galaxies.

To measure the relation, we use the R multidimensional Markov Chain Monte Carlo (MCMC) fitting package HYPER.FIT[1] (Robotham & Obreschkow 2015). Without placing any selection criteria on the data, other than the sigma-cut in *W4* flux already implicit in the PDR data set, we fit a linear relation of the form $\log_{10}(\text{SFR}) = \alpha \log_{10}(M_\star) + \beta$ to the distribution of stellar mass versus SFR, using a Componentwise Hit-and-Run Metropolis MCMC optimization. Using this method, we find a best-fitting linear relationship for the PDR and LDR photometry. Parameters of each of these fits are given in Table 3. Included in these parameters is a value of σ_{orth} per fit, which is the intrinsic scatter orthogonal to the best-fitting line.

Assuming that the relation is in some sense fundamental (i.e. physically motivated), we are able to argue (as we did in Section 6.7) that any reduction in the intrinsic scatter of the fit represents an improvement in the photometry used in determining the fit components. We see a significant reduction in the intrinsic scatter of the fit for the *W4* predictor when using the LDR photometry, and see a consistent scatter when using the 100 μm predictor. However, we note that if we sigma-clip both data sets to 2σ, thus decreasing

Table 3. Fit parameters for the linear relationship between stellar mass and star formation rate, for both the PDR and LDR data sets, when deriving SFRs using predictors based on 100 μm and *W4* fluxes. The upper section of the table shows the fit to all available data, while the lower panel shows the fits when fitting to data with measurements $\geq 2\sigma$. We can see that in each case, the LDR fits and PDR fits are equivalent, but the LDR fit has equivalent or reduced intrinsic scatter. We therefore conclude that the LDR data are a more appropriate representation of the true underlying distribution.

Sample	α	β	σ_{orth}
PDR 100 μm	0.62 ± 0.05	-5.69 ± 0.56	0.225 ± 0.002
LDR 100 μm	0.61 ± 0.04	-5.56 ± 0.36	0.214 ± 0.002
PDR *W4*	0.75 ± 0.06	-6.98 ± 0.68	0.278 ± 0.005
LDR *W4*	0.75 ± 0.08	-7.06 ± 0.85	0.226 ± 0.003
PDR(2σ) 100 μm	0.62 ± 0.04	-5.53 ± 0.43	0.243 ± 0.004
LDR(2σ) 100 μm	0.60 ± 0.02	-5.37 ± 0.23	0.219 ± 0.002

the impact of low significance and possibly spurious measurements, the intrinsic scatter about the fit for the PDR data increases significantly while the LDR intrinsic scatter remains relatively consistent. As such, we conclude that the *W4* and 100 μm photometry in the LDR are both an improvement over the PDR. None the less, the LDR and PDR data sets return equivalent relationships for each predictor. Note however, the substantial improvement in the number of measurements in the MIR means that here we are able to increase our sample from 29 764 estimates in the PDR to 127 524 estimates in the LDR.

8 UPDATING GAMA PHOTOMETRY: DATA RELEASE

In addition to releasing the program, we also release the various data-products that the program outputs for all galaxies in the GAMA equatorial fields. The release is in the form of 24 machine-readable

[1] https://github.com/asgr/hyper.fit

files (.csv), and is accessible via the GAMA Panchromatic Swarp Imager (Ψ) website; http://gama-psi.icrar.org. The 24 files are as follows.

(i) A summary file containing final photometry and uncertainties for all optically defined targets across all 21 bands of photometry.

(ii) Three input catalogues, containing the optical prior aperture information and contaminant lists, as described in Section 6.2.

(iii) 21 individual files containing details specific to the 21 bands in which photometry was measured.

The 21 files containing band-specific information each contain 50 columns, containing information about every objects' sky estimate, blanks measurement, deblend solution, flux measurement, flux iteration, aperture normalization, and any photometry warnings.

9 CONCLUSIONS

In this paper, we have presented a novel program for determining matched aperture photometry across images that are neither pixel- nor PSF-matched. The program is sophisticated enough to reliably analyse imaging from the FUV to the FIR, and produces a substantial number of data products to aid in photometric analysis, quality control, and error handling. We demonstrate that the program is able to return simulated photometric values in both the high SNR, low confusion regime, as well as in the low SNR, high confusion regime. We further demonstrate that the many available subroutines within the program, including (but not limited to) local sky estimation, blanks/randoms correction, object deblending, and iterative flux measurement, behave well in all tested cases.

We run the program over 21 bands of photometry contained within the GAMA survey, and present comparisons between the photometry returned by the program to those in the GAMA PDR (Driver et al. 2016). We demonstrate that the photometry is both broadly consistent with what has come previously, while still being an improvement over previous photometry, as determined by a decrease in the relative widths of colour distributions across facility boundaries, an increase in the number of measurements, and greater consistency and reliability of uncertainties.

By fitting SEDs to the optical and NIR photometry, we are able to measure stellar masses for all galaxies in our sample. We compare stellar mass estimates derived from the GAMA PDR photometry to those derived from the LAMBDAR photometry, finding median residual between the mass estimates of -0.004 ± 0.030 dex.

Using the LAMBDAR program, we are able to increase the rate of measurements in low-sensitivity images by forcing photometric measurements at optically motivated positions. Using the program, for example, we make measurements in the *WISE W*4 band at the position of every GAMA target. The result is an increase in the number of measurements, but also a systematic increase in the range of colours able to be probed in the *WISE* bands.

Using these stellar mass estimates and star formation rate indicators derived from *Herschel* PACS 100 μm and *WISE W*4 luminosities, we measure a linear fit to the star formation rate main sequence using the R multidimensional Markov-Chain Monte Carlo fitting package HYPER.FIT (Robotham & Obreschkow 2015). Comparing the relations we derive using each predictor, for both the PDR and LDR data sets, we find good agreement. We note, however, that the relation derived using the LDR data set demonstrates a decrease in the intrinsic scatter about the star formation rate main sequence, indicating a reduction in random errors.

From these tests, we conclude that the LAMBDAR photometry is indeed superior to that derived by table matching.

Finally, we detail the data release to accompany this paper. Photometry measured using LAMBDAR has been made available through the GAMA Panchromatic Swarp Imager (Ψ) website; http://gama-psi.icrar.org/, along with many relevant subproducts detailed here. These include sky estimates, deblend fractions, normalization factors, and more.

REFERENCES

Abazajian K. N. et al., 2009, ApJS, 182, 543
Andrae E., 2014, PhD thesis, Max-Planck-Institut für Kernphysik
Baldry I. K. et al., 2012, MNRAS, 421, 621
Bertin E., Arnouts S., 1996, A&AS, 117, 393
Bertin E., Mellier Y., Radovich M., Missonnier G., Didelon P., Morin B., 2002, in Bohlender D. A., Durand D., Handley T. H., eds, ASP Conf. Ser. Vol. 281, Astronomical Data Analysis Software and Systems XI. Astron. Soc. Pac., San Francisco, p. 228
Boquien M. et al., 2013, A&A, 554, A14
Bourne N. et al., 2012, MNRAS, 421, 3027
Bourne N. et al., 2016, in press
Brown M. J. I. et al., 2014, ApJS, 212, 18
Bundy K., Hogg D. W., Higgs T. D., Nichol R. C., Yasuda N., Masters K. L., Lang D., Wake D. A., 2012, AJ, 144, 188
Cameron E., 2011, PASA, 28, 128
Camps P., Baes M., 2015, Astron. Comput., 9, 20
Capak P. et al., 2007, ApJS, 172, 99
Cluver M. E. et al., 2014, ApJ, 782, 90
Conroy C., 2013, ARA&A, 51, 393
Da Cunha E., Charlot S., 2011, Astrophysics Source Code Library, record ascl:1106.010

[2] https://cran.r-project.org/package=magicaxis

Da Cunha E., Charlot S., Elbaz D., 2008, MNRAS, 388, 1595
Davies L. J. M. et al., 2015, MNRAS, 452, 616
Davies L. J. M. et al., 2016, MNRAS, 455, 4013
De Santis C., Grazian A., Fontana A., Santini P., 2007, New Astron., 12, 271
De Vaucouleurs G., 1948, Ann. Astrophys., 11, 247
Driver S. P. et al., 2011, MNRAS, 413, 971
Driver S. P. et al., 2016, MNRAS, 455, 3911
Dunne L. et al., 2011, MNRAS, 417, 1510
Eales S. et al., 2010, PASP, 122, 499
Elbaz D. et al., 2011, A&A, 533, A119
Erwin P., 2014, Astrophysics Source Code Library, record ascl:1408.001
Freeman K. C., 1970, ApJ, 160, 811
Graham A. W., Driver S. P., Petrosian V., Conselice C. J., Bershady M. A., Crawford S. M., Goto T., 2005, AJ, 130, 1535
Griffin M. J. et al., 2010, A&A, 518, L3
Grogin N. A. et al., 2011, ApJS, 197, 35
Hildebrandt H. et al., 2012, MNRAS, 421, 2355
Hill D. T., Driver S. P., Cameron E., Cross N., Liske J., Robotham A., 2010, MNRAS, 404, 1215
Hill D. T. et al., 2011, MNRAS, 412, 765
Jarrett T. H., Chester T., Cutri R., Schneider S., Skrutskie M., Huchra J. P., 2000, AJ, 119, 2498
Jarrett T. H. et al., 2012, AJ, 144, 68
Jarrett T. H. et al., 2013, AJ, 145, 6
Kelvin L. S. et al., 2012, MNRAS, 421, 1007
Kelvin L. S. et al., 2014, MNRAS, 439, 1245
Koekemoer A. M. et al., 2011, ApJS, 197, 36
Kron R. G., 1980, ApJS, 43, 305
Kuijken K., 2008, A&A, 482, 1053
Lacey C. G. et al., 2015, preprint (arXiv:1509.08473)
Laidler V. G. et al., 2007, PASP, 119, 1325
Liske J., Lemon D. J., Driver S. P., Cross N. J. G., Couch W. J., 2003, MNRAS, 344, 307

Liske J. et al., 2015, MNRAS, 452, 2087
Madau P., Dickinson M., 2014, ARA&A, 52, 415
Mancone C. L., Gonzalez A. H., Moustakas L. A., Price A., 2013, PASP, 125, 1514
Martin A. M., Papastergis E., Giovanelli R., Haynes M. P., Springob C. M., Stierwalt S., 2010, ApJ, 723, 1359
Merlin E. et al., 2015, A&A, 582, A15
Morrissey P. et al., 2007, ApJS, 173, 682
Oliver S. J. et al., 2012, MNRAS, 424, 1614
Papastergis E., Cattaneo A., Huang S., Giovanelli R., Haynes M. P., 2012, ApJ, 759, 138
Patterson F. S., 1940, Harv. Coll. Obs. Bull., 914, 9
Petrosian V., 1976, ApJ, 209, L1
Pilbratt G. L. et al., 2010, A&A, 518, L1
Poglitsch A. et al., 2010, A&A, 518, L2
Popescu C. C., Tuffs R. J., Dopita M. A., Fischera J., Kylafis N. D., Madore B. F., 2011, A&A, 527, A109
R Core Team 2015, R: A Language and Environment for Statistical Computing. R Foundation for Statistical Computing, Vienna, Austria, Available at: https://www.R-project.org/
Robotham A. S. G., Obreschkow D., 2015, PASA, 32, e033
Scoville N. et al., 2007, ApJS, 172, 1
Sérsic J. L., 1963, Bol. Asociacion Argentina Astron., 6, 41
Strauss M. A. et al., 2002, AJ, 124, 1810
Sutherland W. et al., 2015, A&A, 575, A25
Taylor E. N. et al., 2011, MNRAS, 418, 1587
Vaccari M., HELP Consortium T., 2015, preprint (arXiv:1508.06444)
Valiante et al., 2016, in press
Vika M., Bamford S., Häußler B., Rojas A., 2013, Mem. Soc. Astron. Ital. Suppl., 25, 41
Walcher J., Groves B., Budavári T., Dale D., 2011, Ap&SS, 331, 1
Wang L. et al., 2014, MNRAS, 444, 287
Wright E. L. et al., 2010, AJ, 140, 1868
York D. G. et al., 2000, AJ, 120, 1579

APPENDIX A: SKY ESTIMATES AND NEBULIZER

Comparison between low-level variations as measured by LAMBDAR's sky estimation routine and as measured by the nebulizer routine presented in Valiante et al. (2016). Fig. A1 shows the two estimates as a function of RA/DEC. Here, the LAMBDAR measurements were made by running the sky estimate routine cen-

tred on every pixel in the image, *without* masking of known targets, using a single 3σ clip, and with annuli between 17 and 60 pixels ($\sim$1 to 3 arcmin) in radius. These annuli are shown graphically (in black) in the bottom right of each LAMBDAR panel, along with the PSF FWHM (in red). From these figures, we conclude that the sky estimate routine is a sufficiently capable tool of removing subtle variations in the background in the absence of a removal by nebulizer.
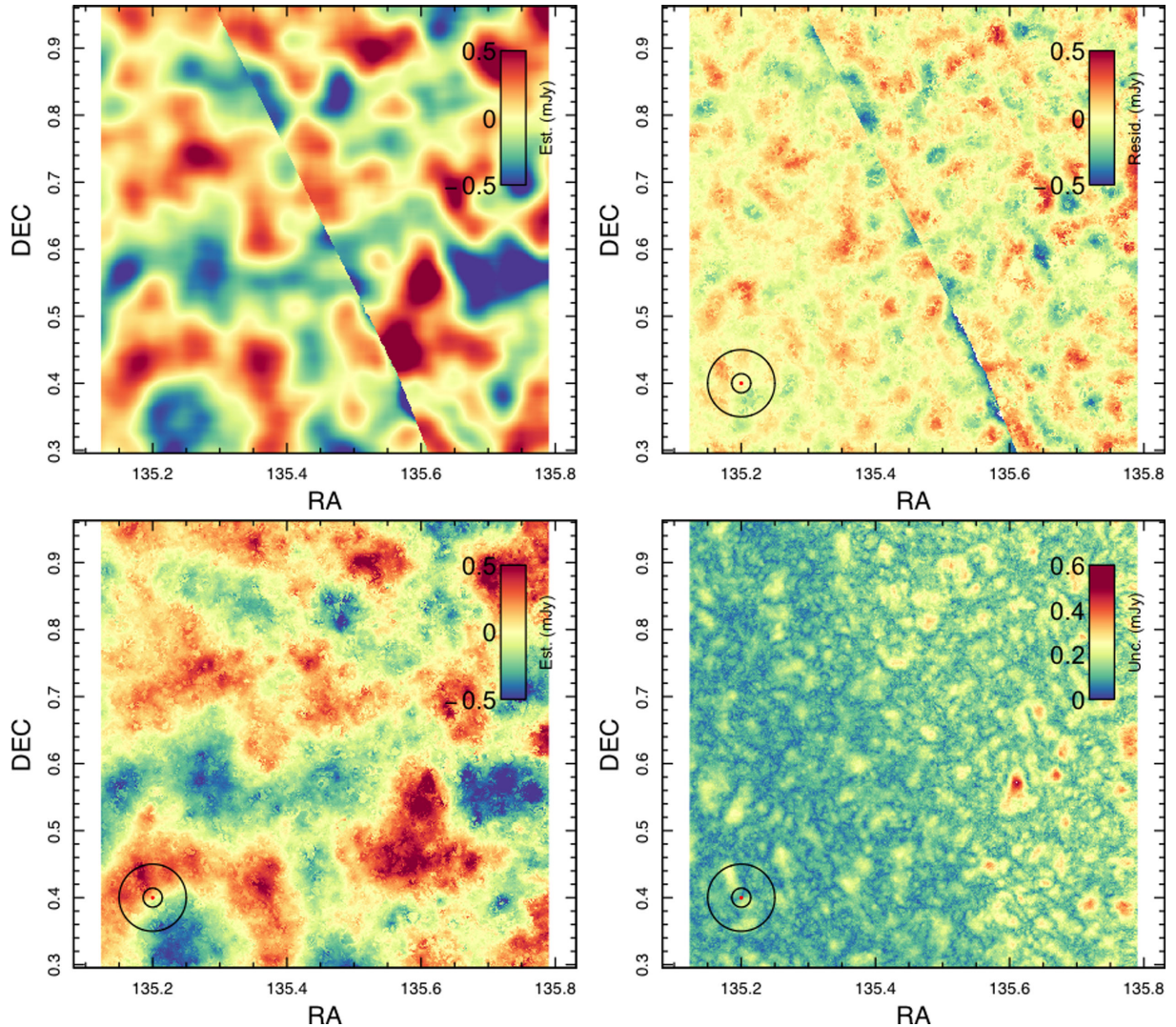
Figure A1. Comparison between the small background variations in a subregion of the G09 PACS 100 μm mosaic, as measured by nebulizer (top left) with those measured by the LAMBDAR sky estimate (bottom left). The residual between the two estimates is shown in the top-right panel, and the uncertainty on the LAMBDAR measurement is shown in the bottom right. The diagonal discontinuity in the nebulizer distribution lies along the boundary of two frames. Because of the frame-overlap, there is single-depth data to the right of the join, and double-depth data to the left of the join. This is reflected in the LAMBDAR uncertainty panel, where uncertainties are systematically higher. In each of the LAMBDAR panels, a graphic demonstration of the annuli used in measuring the sky is shown (in black) in the bottom left. The PSF FWHM is also shown (in red), for reference.

APPENDIX B: FLUX ITERATION AND DEBLENDING

The outcome of iterative deblending and flux determination for a range of simulated flux ratios. Note that, as (in these tests) we always begin (iteration 0) from a state where the model flux ratio is unity, we will always converge from the same direction: bright objects will begin seemingly dimmer, and dim objects will begin seemingly brighter. The result of this is that our final fluxes will, in cases
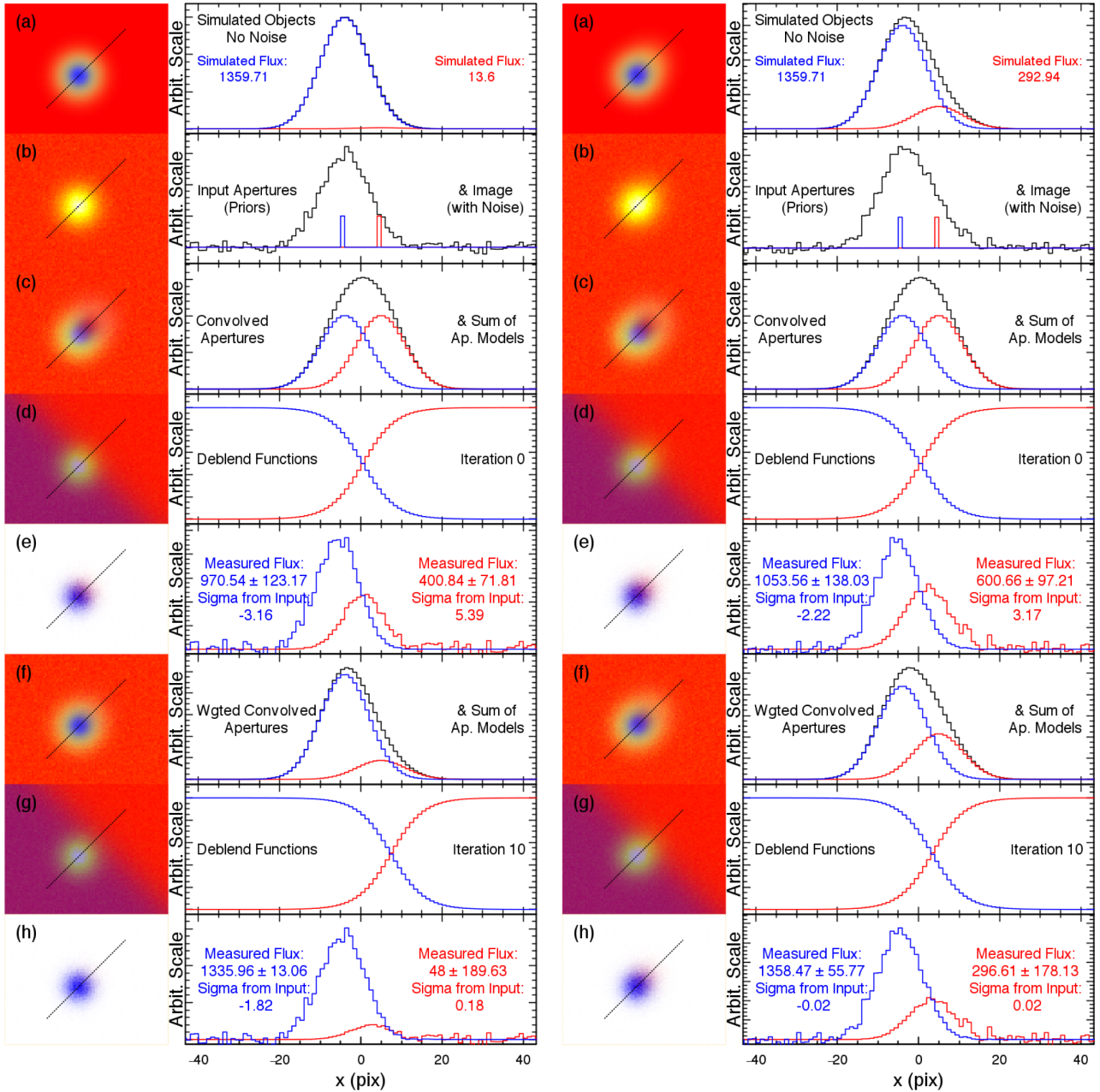
Figure B1. Iterative deblending of complex sources in LAMBDAR. The rows of each figure show: the two simulated objects (red and blue, respectively) and the total flux profile (black), before addition of noise (row 'a'); the simulated total flux profile after addition of noise (black), and the apertures provided to the LAMBDAR program (red and blue; row 'b'); the convolved apertures and their sum with no weighting applied (red, blue, and black, respectively; row 'c'); the iteration 0 deblend functions for the red and blue sources, determined using the distributions from the panel above (row 'd'); the simulated image multiplied by the iteration 0 deblend functions (this is the so-called deblended images), for the red and blue sources, respectively. Also shown are the measured fluxes and uncertainties at iteration 0 (row 'e'); the iteration 10 weighted convolved apertures for the red and blue sources, and their sum (row 'f'); the iteration 10 deblend function (row 'g'); the iteration 10 deblended images, and the measured iteration 10 fluxes with uncertainties (row 'h'). In these two simulations, two point sources have been simulated with very different fluxes. In the left-hand panel, the source shown in blue has simulated flux 100 times brighter than the companion source, shown in red. In the right-hand panel, the blue source has flux ~5 times brighter than the companion source. In the first case, the program is unable to converge (within uncertainties) in 10 iterations; this highlights the problem of providing catalogues that are too deep for the imaging under analysis. In the second case however, despite the two sources being very different in their respective brightnesses, the program converges to within uncertainties within the 10 iterations shown here.
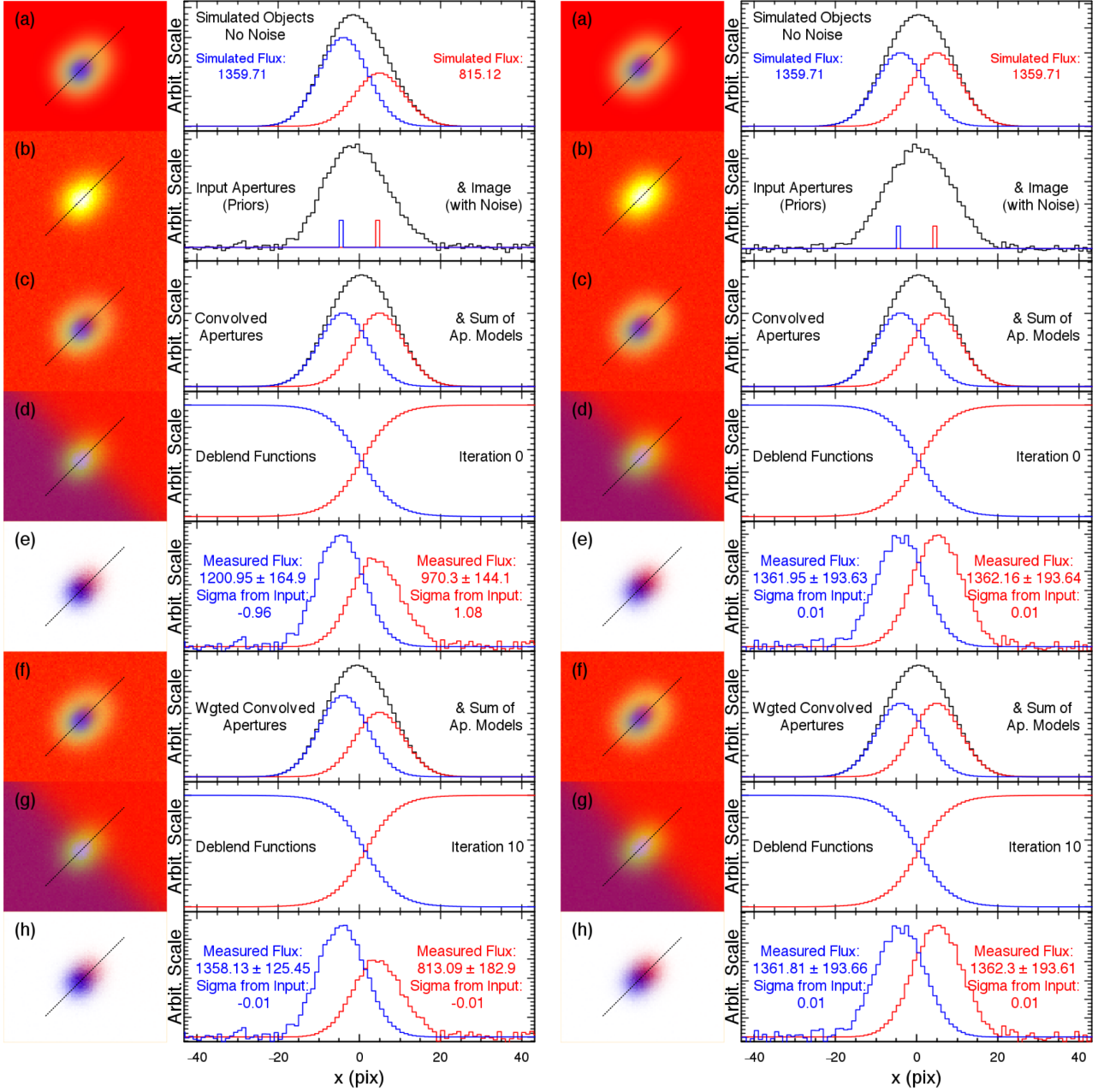
Figure B2. Figure B1 continued. In these two simulations the blue source has flux that is ∼1.5 times brighter (left) and equal to the companion (right). Again, the program converges to the solution within uncertainties within the 10 iterations.

of highly non-unity flux ratios, tend to underestimate the brighter object's flux and overestimate the dimmer object's flux. Importantly, these tests showcase that deblending of unresolved sources with flux ratio <0.02 typically does not converge to a correct solution within 10 iterations.

APPENDIX C: COMPARISONS TO GAMA PDR

Here we show the full comparisons between the GAMA PDR photometry and that derived from the program. Note that in all of these figures, photometry has been calculated with the parameters detailed in Table 2, running LAMBDAR version 0.14. Included here are trumpet plots (Fig. 20), colour distributions (Fig. 24), and error components (Fig. 23), for all 21 photometric bands.
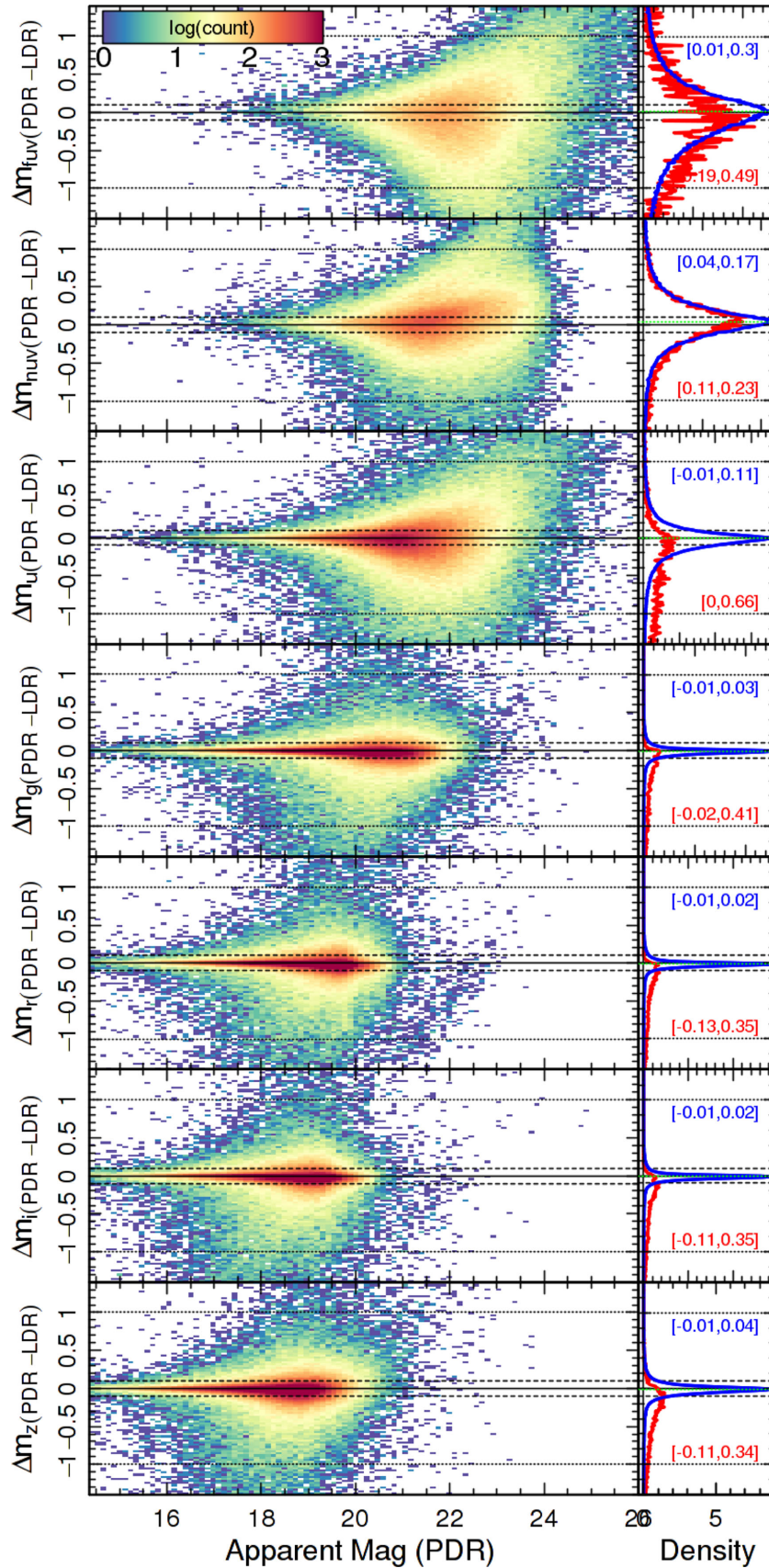
Figure C1. Trumpet plots for the full 21-band photometry in GAMA. The left-hand column is the same as Fig. 20. The right-hand column shows the projected distribution of residuals, split into resolved sources (blue), and point sources (red). The mode and RMS of each distribution is also shown for each of the projected density distributions, in blue and red. Horizontal solid, dashed, and dotted lines show the 0, 0.1, and 1 mag residual points, for reference.
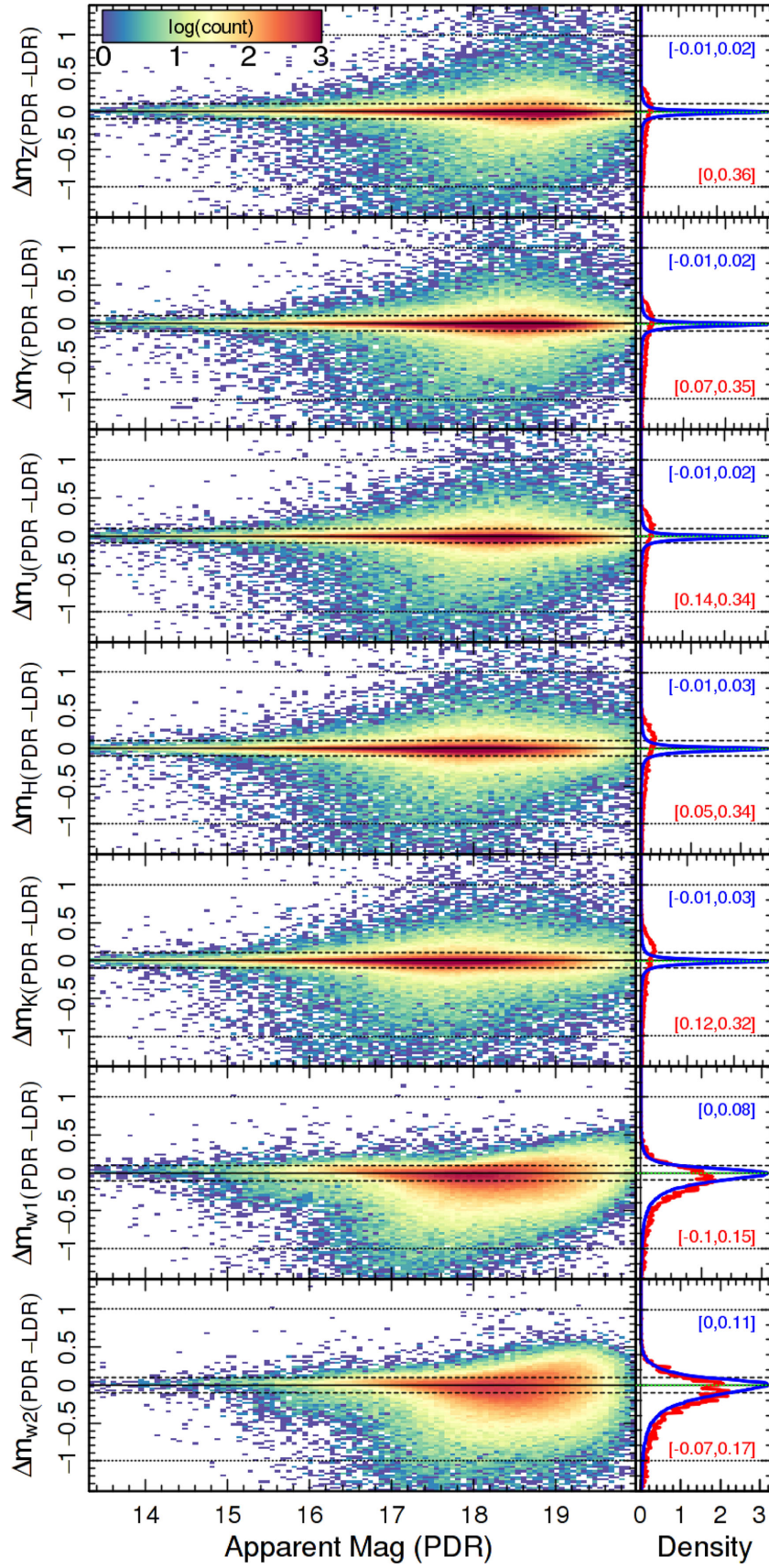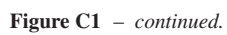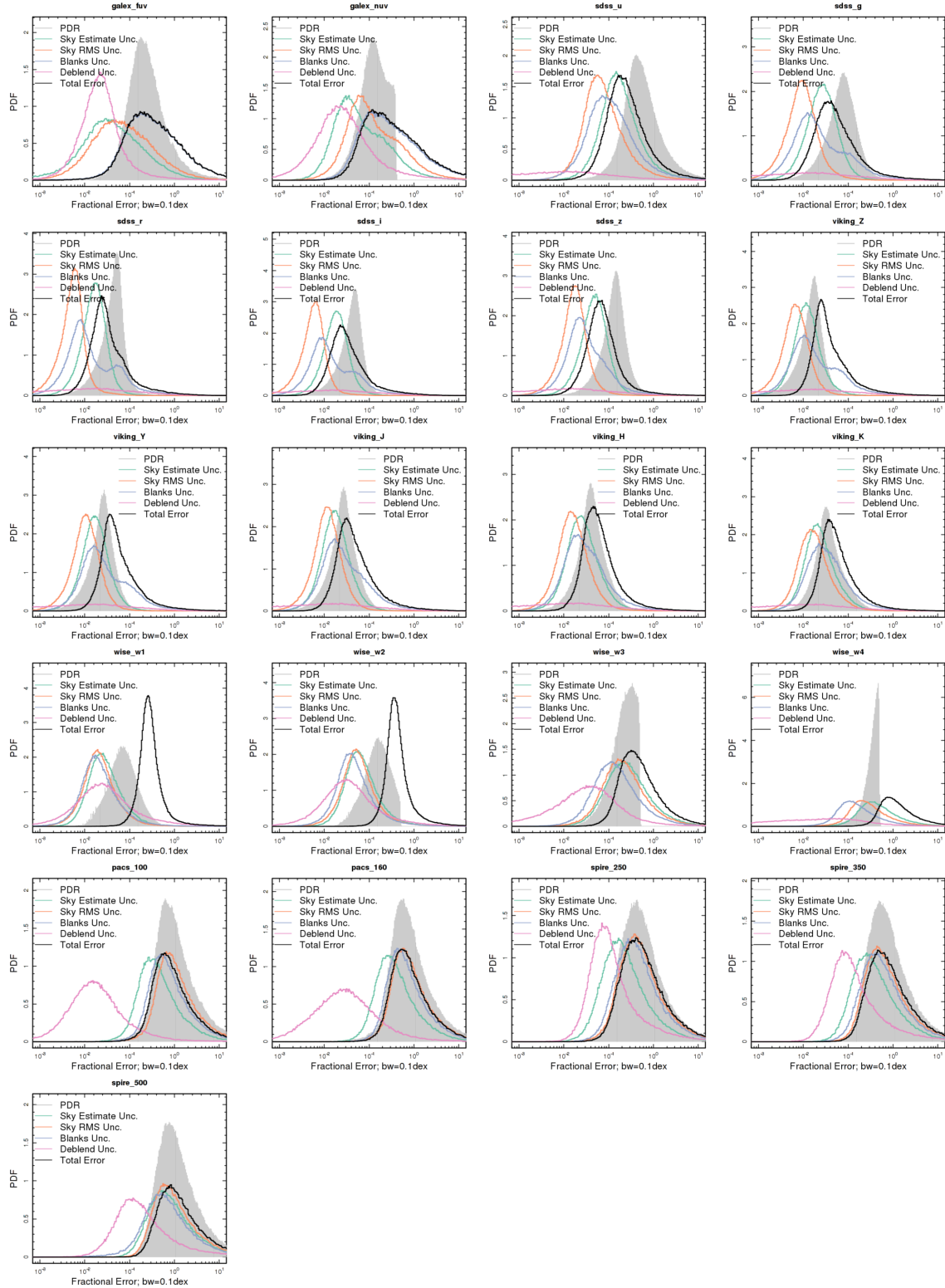
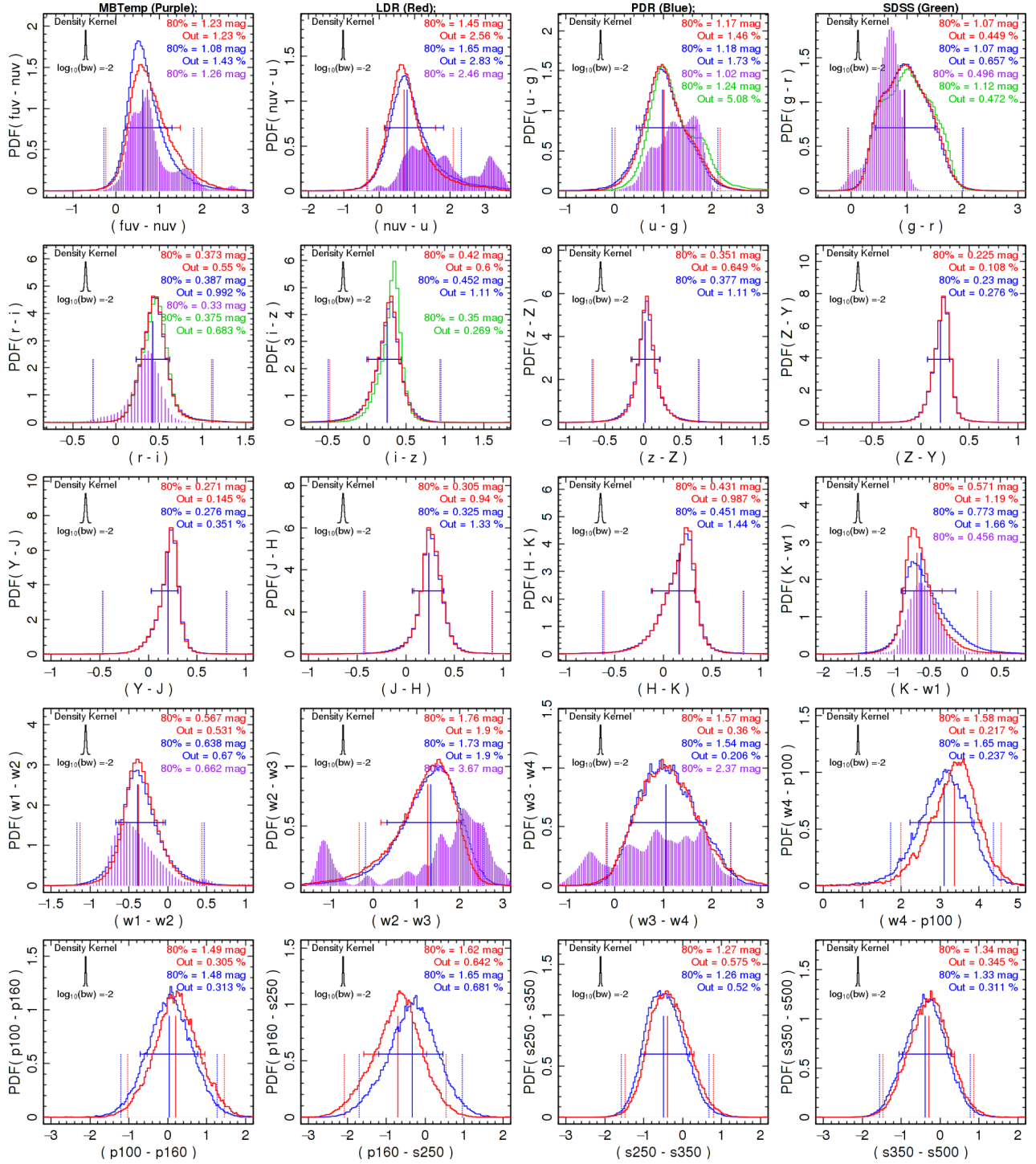**Figure C1** – *continued.*

Figure C1 – *continued.*

Figure C2. Error distributions for the full 21-band photometry in GAMA. Details of the panels are given in the caption of Fig. 23.

Figure C3. Colour distributions for the full 21-band photometry in GAMA. Details of the panels are given in the caption of Fig. 24.

[1]*ICRAR[†], The University of Western Australia, 35 Stirling Highway, Crawley, WA 6009, Australia*

[2]*SUPA, Institute for Astronomy, University of Edinburgh, Royal Observatory, Blackford Hill, Edinburgh EH9 3HJ, UK*

[3]*SUPA, School of Physics and Astronomy, University of St Andrews, North Haugh, St Andrews, Fife KY16 9SS, UK*

[4]*School of Physics and Astronomy, Cardiff University, The Parade, Cardiff CF24 3AA, UK*

[5]*NASA Ames Research Center, N232, Moffett Field, Mountain View, CA 94035, USA*

[6]*Australian Astronomical Observatory, PO Box 915, North Ryde, NSW 1670, Australia*

[7]*Sydney Institute for Astronomy, School of Physics A28, University of Sydney, NSW 2006, Australia*

[8]*School of Physics and Astronomy, Monash University, Clayton, VIC 3800, Australia*

[9]*Astronomy Centre, University of Sussex, Falmer, Brighton BN1 9QH, UK*

[10]*Department of Physics and Astronomy, University of the Western Cape, Robert Sobukwe Road, Bellville 7535, South Africa*

[11]*ESA/ESTEC, Keplerlaan 1, NL-2201 AZ Noordwijk, The Netherlands*

[12]*University of Leiden, Sterrenwacht Leiden, Niels Bohrweg 2, NL-2333 CA Leiden, the Netherlands*

[13]*Astronomy Dept, University of Cape Town, Rondebosch 7701, RSA*

[14]*Hamburger Sternwarte, Universität Hamburg, Gojenbergsweg 112, D-21029 Hamburg, Germany*

[15]*ICC and CEA, Department of Physics, Durham University, South Road, Durham DH1 3LE, UK*

[16]*Jeremiah Horrocks Institute, University of Central Lancashire, Preston PR1 2HE, UK*

[17]*The Astronomical Institute of the Romanian Academy, Str. Cutitul de Argint 5, Bucharest, Romania*

[18]*School of Physics, the University of Melbourne, VIC 3010, Australia*

[19]*Max Planck Institut fuer Kernphysik, Saupfercheckweg 1, D-69117 Heidelberg, Germany*

[20]*SRON Netherlands Institute for Space Research, Landleven 12, NL-9747 AD Groningen, the Netherlands*

[†]International Centre for Radio Astronomy Research

This paper has been typeset from a TEX/LATEX file prepared by the author.